7

Protein–Ligand Interaction Probed by Time-Resolved Crystallography

Marius Schmidt, Hyotcherl Ihee, Reinhard Pahl, and Vukica Šrajer

Summary

Time-resolved (TR) crystallography is a unique method for determining the structures of intermediates in biomolecular reactions. The technique reached its mature stage with the development of the powerful third-generation synchrotron X-ray sources, and the advances in data processing and analysis of time-resolved Laue crystallographic data. A time resolution of 100 ps has been achieved and relatively small structural changes can be detected even from only partial reaction initiation. The remaining challenge facing the application of this technique to a broad range of biological systems is to find an efficient and rapid, system-specific method for the reaction initiation in the crystal. Other frontiers for the technique involve the continued improvement in time resolution and further advances in methods for determining intermediate structures and reaction mechanisms. The time-resolved technique, combined with trapping methods and computational approaches, holds the promise for a complete structure-based description of biomolecular reactions.

Key Words: Time-resolved macromolecular crystallography; Laue diffraction; intermediate states; reaction mechanism; SVD.

1. Introduction

Studies of macromolecules by X-ray diffraction technique over the last few decades provided an enormous wealth of information on three-dimensional structures of protein, DNA and RNA molecules. These average, static three-dimensional pictures of macromolecules offer a significant insight into their function. However, to fully understand how these molecules perform their function one has to watch them in action, along a reaction path that often involves short-lived intermediates. Many such reactions are possible in crys-

From: *Methods in Molecular Biology, vol. 305: Protein–Ligand Interactions: Methods and Applications*
Edited by: G. U. Nienhaus © Humana Press Inc., Totowa, NJ

tals as they typically contain a large percentage of solvent, about 40 to 60%. The solvent forms channels and hydration shells around protein molecules and facilitates dynamic processes such as diffusion and binding of substrates and other ligands, turn-over in enzyme crystals, and conformational change in response to absorption of light in photoreceptors. Crystallography can, therefore, also play an important role in visualizing structures of reaction intermediates and elucidating reaction mechanism. The term time-resolved X-ray crystallography (TRX) is sometimes used in a broad sense to encompass a variety of methods that investigate structural intermediates. Trapping methods are often used to extend the lifetime of intermediate species and increase their peak concentration. Physical trapping can be accomplished by conducting a reaction at low temperature (freeze-trapping). Or alternatively, a reaction can be initiated at room temperature and a particular intermediate trapped at a certain time delay after the reaction initiation by rapid cooling (trap-freezing). Chemical trapping can be achieved by a pH change, by site-directed mutagenesis, or by chemical modification of the substrate or cofactor. Although the trapping strategy alters to some degree the reaction and structures of intermediates that are investigated, such methods are nevertheless attractive. These experiments can be conducted using the standard monochromatic oscillation technique and important information about reaction pathways and intermediates can be obtained ***(1–4)***. A more direct, but also technically more challenging strategy to study intermediates, is to utilize the TRX in a strict sense of the term and to follow the unperturbed reaction as it evolves at room temperature. We will focus here on the principles, challenges, and applications of such, more narrowly defined TRX.

TR crystallography and TR spectroscopy share the same goal: revealing the reaction mechanism and structural characteristics of intermediate states. The main advantage of TRX is that detailed structural information is obtained directly and globally, for the entire molecule. Spectroscopic techniques, such as visible or UV absorption, resonance Raman, and IR spectroscopy can be very sensitive to small structural changes but typically provide local structural information indirectly. In some cases, like with the IR amide I band, overall global information is obtained. Although the time course of spectroscopic changes reflects the time course of tertiary structural changes ***(5–12)***, it is often difficult to unambiguously link spectroscopic changes to particular and specific underlying structural changes, and to relate the amplitude of spectroscopic change to the extent of structural change. However, the two techniques are complementary and taken together provide a more complete insight into structural changes and reaction mechanism.

In TRX experiments, one triggers a reaction in molecules in the crystal and uses X-ray pulses to probe structural changes at various time delays following

the start of the reaction. The time resolution of the experiment is determined by either the duration of the triggering process or the duration of the X-ray probe pulse, whichever is longer. Experiments require synchrotron X-ray radiation. Synchrotrons are pulsed X-ray sources with a typical X-ray pulse duration of about 100 ps. When longer X-ray exposures are sufficient, a train of X-ray pulses of appropriate duration can be used (*see* **Subheading 3.3.**). The best time resolution achieved to date matches the duration of a single X-ray pulse ***(13)***. Very high X-ray flux is needed to obtain data of necessary quality with ns and sub-ns time resolution. Third-generation synchrotron sources ***(14)*** provide the most intense X-ray pulses to date. Such sources are the Advanced Photon Source (APS) (USA), European Synchrotron Radiation Facility (ESRF) (France), and SPring-8 (Japan).

Experiments that require subsecond time resolution have to be conducted at synchrotron facilities with polychromatic beam capability. It is impossible to record the integral intensity of a reflection in such a short exposure time using the conventional monochromatic method where the crystal has to be rotated/oscillated. The polychromatic, Laue X-ray diffraction technique is used instead, where the crystal is stationary ***(15)***. Bending magnet beamlines are sufficient for experiments that require ms time resolution, whereas insertion device beamlines ***(14)*** are necessary for sub-ms resolution.

A comprehensive review of the present state of the Laue technique as well as examples of its application to static and TR studies can be found in **ref. *15***. The technique has reached a mature stage. Most of the problems in Laue data processing, that limited the use of this technique in the past, have been solved. Structure factor amplitudes from static Laue experiments equal in quality those from standard monochromatic oscillation measurements.

Reaction triggering is a crucial and critical part of TRX experiments and will be discussed in more detail in **Subheadings 3.2.** and **3.4.** Ideally, the triggering is accomplished rapidly in all molecules in the crystal, in a time interval much shorter than the lifetime of the intermediate that is investigated and the duration of the X-ray pulse used to probe the intermediate. In reality, triggering occurs only in a fraction of molecules. One of the experimental goals is to maximize this fraction. The fastest method for triggering a reaction in the crystal is to use ultrashort, fs to ns, laser pulses. The method can be applied to photosensitive molecules that undergo structural changes upon the absorption of light by an embedded chromophore. Examples, extensively studied by TR spectroscopy, include heme proteins ***(13,16–18)***, bacteriorhodopsin ***(19)***, photoactive yellow protein ***(5,20–22)***, and other photoreceptors ***(23)***. We will focus here mainly on TRX studies of such inherently photosensitive proteins.

The readout speed of present large area X-ray detectors used for macromolecular crystallography does not permit to follow the subsecond reactions in

real time after a single reaction initiation. Collecting a diffraction image at each time delay, therefore, requires a separate reaction initiation event. In addition, multiple diffraction images at different crystal orientations are needed for a complete data set at each time delay (*see* **Subheading 3.4.**). It is therefore greatly advantageous if the reaction is reversible and the system restores itself to the initial state after a relatively short period of time. For such systems, a single crystal can be used for collecting complete or even multiple data sets. Processes where the triggering step or the reaction itself is irreversible can also be studied in favorable cases, but a new crystal is required for each X-ray exposure.

The result of a pump-probe TRX measurement is a four-dimensional data set, consisting of a time series of structure factor (SF) amplitudes, $|\mathbf{F}(hkl,t)|$. Because the goal is to determine how the known initial structure is changing in time following the reaction initiation, we are actually interested in the difference between the time-dependent SF amplitudes $|\mathbf{F}(hkl,t)|$ and the SF amplitudes corresponding to the initial state, $|\mathbf{F}(hkl)|$. Results are typically presented in real space (x,y,z) rather than reciprocal (h,k,l) space. Time-dependent difference electron density (DED) maps, $\Delta\rho(t)$, are calculated on a three-dimensional grid across the crystal unit cell, with coefficients $\Delta F(h,k,l,t) = |\mathbf{F}(hkl,t)|-|\mathbf{F}(hkl)|$ and phases obtained from the structure of the initial state (*see* **Subheading 3.5.2.**). DED maps are analogous to difference spectra in TR spectroscopy. Negative densities in such maps represent the loss of electrons and positive densities the gain of electrons. A DED that results from a structural change varies relatively smoothly with time when determined with a sufficiently high signal-to-noise ratio (SNR).

Many chemical reactions are considered *simple* ***(24,25)*** and can be represented by a chemical kinetic model where the reaction proceeds along a reaction coordinate and involves a set of discrete intermediate states I_j. These states correspond to the minima on the potential energy surface of the system. They are separated by well-defined energy barriers and the interconversion between them follows exponential behavior. To fully describe the kinetic mechanism one then needs to determine the number of intermediate states, the pathways by which they interconvert, and the rate coefficients of their interconversion (**Fig. 1**). When these are known, the kinetics of the ensemble of molecules in the crystal can be described. Following the reaction initiation, molecules populate intermediate states according to fractional (normalized) concentrations, $I_j(t)$, which are governed by a system of coupled differential equations that describes a given mechanism (**Fig. 2**). Each molecule crosses the energy barrier between the states I_j at random and independently from other molecules, and spends a short time in the transition state (at the top of the barrier) as compared to the residence time in I_j states. An intermediate state can in prin-

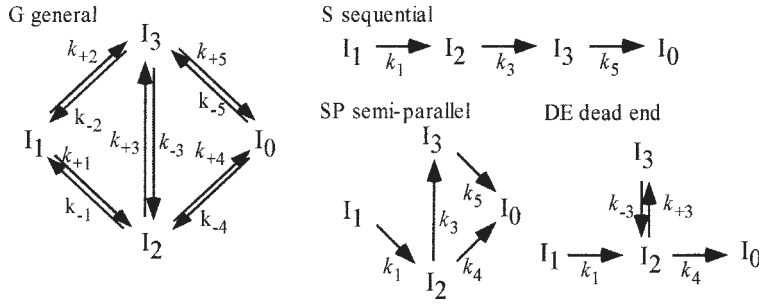

Fig. 1. General mechanism (G) with three intermediate states: I_1, I_2, and I_3. The final state is I_0. In a reversible system this is also the initial state. Three simple mechanisms (S, SP, DE) based on three intermediates are also shown.

A

$$\frac{dI_1}{dt} = -k_1 I_1$$

$$\frac{dI_2}{dt} = k_1 I_1 - k_{+4} I_2 - k_{+3} I_2 + k_{-3} I_3$$

$$\frac{dI_3}{dt} = k_{+3} I_2 - k_{-3} I_3$$

$$I_1 + I_2 + I_3 + I_0 = 1$$

B

$$I_1 = P_{11} e^{\lambda_1 \cdot t} + P_{12} e^{\lambda_2 \cdot t} + P_{13} e^{\lambda_3 \cdot t}$$

$$I_2 = P_{21} e^{\lambda_1 \cdot t} + P_{22} e^{\lambda_2 \cdot t} + P_{23} e^{\lambda_3 \cdot t}$$

$$I_3 = P_{31} e^{\lambda_1 \cdot t} + P_{32} e^{\lambda_2 \cdot t} + P_{33} e^{\lambda_3 \cdot t}$$

Fig. 2. Chemical kinetic model: fractional concentrations of intermediates for mechanism DE in **Fig. 1**. **(A)** Three differential equations describe the mechanism. I_1, I_2, I_3: time-dependent fractional concentrations of molecules populating the intermediate states I_1, I_2, and I_3. The forth equation (sum of all fractional concentration is 1) determines the concentration of the I_0 state. **(B)** General solution of differential equations in (A). Relaxation rate coefficients λ_i are the same for all intermediates and exclusively depend on the rate coefficients k (inverse of $|\lambda_i|$ are relaxation times, $\tau_i = 1/|\lambda_i|$). The λ_i are directly observable, the k are not. The pre-exponentials P_{ji} depend on initial conditions and λ_i, and therefore also depend on the rate coefficients k (*see* ***25a*** for illustrative examples). The three exponential terms in the expression for each intermediate are called transients.

ciple be significantly populated at some time delay, depending on the values of the interconversion rate coefficients (**Fig. 3**). Structural changes can be visualized as hopping of molecules between structurally distinct intermediate states I_j. In other words, what changes in time are the fractional concentrations of molecules in various intermediate states. As a result, TRX experiments do not produce a movie of continuously changing structure, but a set of discrete structures corresponding to the intermediate states.

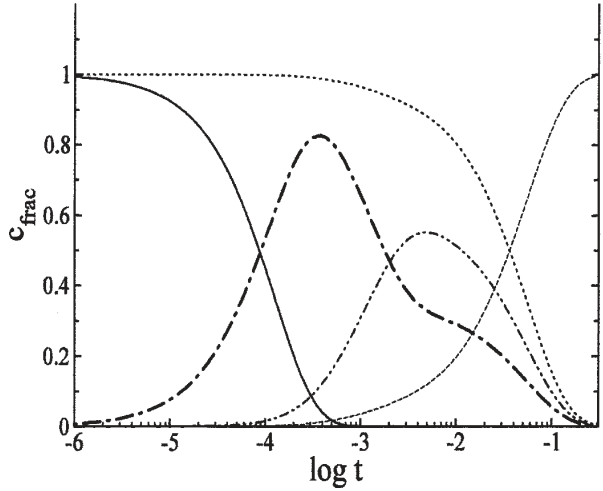

Fig. 3. Calculated fractional concentrations of molecules populating the three intermediate states: I_1 (solid line), I_2 (dot-dashed line), I_3 (double dot-dashed line), and the final state I_0 (dashed line) for the mechanism DE shown in **Figs. 1** and **2**. Reaction triggering is assumed instantaneous and all molecules are in state I_1 at $t = 0$. The sum of I_1, I_2, and I_3 is shown as dotted line. Rate coefficients: $k_1 = 8000\ s^{-1}$, $k_{+3} = 500\ s^{-1}$, $k_{-3} = 300\ s^{-1}$, $k_{+4} = 50\ s^{-1}$. Note a logarithmic time scale.

How does the chemical kinetic model apply to the results of TRX measurements? The DED at each grid point m in a DED map at a given time delay t after the reaction initiation, $\Delta\rho(t)_m$, can be represented by **Eq. 1**:

$$\Delta\rho(t)_m = \sum_{j=1}^{N} I_j(t) \cdot \Delta\rho_{j,m} \tag{1}$$

where $I_j(t)$ is the time-dependent fractional concentration of molecules in the intermediate state I_j, and $\Delta\rho_{j,m}$ is the DED corresponding to a pure intermediate state I_j. Note that the electron densities, but not the measured SF amplitudes $|\mathbf{F}(hkl,t)|$, are proportional to the fractional concentrations ***(26,27)***. Therefore, the analysis should be performed in real space (electron density), rather than reciprocal space (SF amplitudes). Also, note that in general at most delay times several intermediates may be present **(Fig. 3)** and measured DEDs represent a mixture of these intermediate states. Methods for separating the measured mixtures of states $\Delta\rho(t)$ into DEDs $\Delta\rho_j$ of the component intermediate states, and ultimately determining the structures of these intermediate states, have been developed recently ***(27–29)*** and are described in detail in **Subheading 3.5.**

2. Materials

2.1. Time-Resolved X-Ray Diffraction Experiments

1. Crystals.
2. Thin-walled glass or quartz capillaries for crystal mounting and other crystal mounting tools *(30,31)*.
3. A crystal-cooling device (such as the FTS Air-Jet crystal cooler) to maintain constant crystal temperature.
4. Suitable caged compounds for triggering the reaction in crystals that are not inherently photosensitive.
5. A laser for reaction initiation. The following has to be considered when deciding what type of laser to use: wavelength, pulse energy, repetition rate, and pulse duration. The choice will depend on the properties of the sample and the desired time resolution.
6. Optical fibers and/or other optics necessary for delivering the laser light to the sample.
7. A microspectrophotometer for measuring crystal absorption spectra and preliminary TR spectroscopy on crystals. Appropriate light sources for monitoring absorption and reaction initiation have to be considered depending on the absorption properties of the sample.
8. Polychromatic synchrotron X-ray source.
9. Fast and slow X-ray shutters for selecting and isolating individual X-ray pulses or pulse trains.
10. Timing electronics for synchronization of laser and X-ray pulses. The synchronization jitter has to be smaller than the laser or X-ray pulse duration, whichever is longer. Delay generators are needed for adjusting the time delay between laser and X-ray pulses. PIN diodes are generally used for detecting laser and X-ray pulses at the sample location and a fast oscilloscope for measuring the time delay between these pulses.
11. A large area detector for recording diffraction patterns. Image plate or CCD detectors are required to provide sufficient sensitivity.

2.2. Processing and Analysis of Time-Resolved Data

1. Laue data processing. Several software packages are available: LaueView *(32,33)*, Daresbury Laboratory Laue Software Suite (Lauegen, Lscale) *(34,35)*, Leap *(36)*, PrOW *(37)*, Precognition *(38)*.
2. Analysis of DED maps. Integration of DED features: Probe *(16)*; SVD analysis: SVD4TX, GetMech *(27,28)*.

3. Methods

3.1. Sample Preparation

Crystal requirements for TR Laue experiments are more stringent than for the standard, monochromatic oscillation data collection. The Laue technique is more sensitive to crystal mosaicity. Laue diffraction spots become elongated

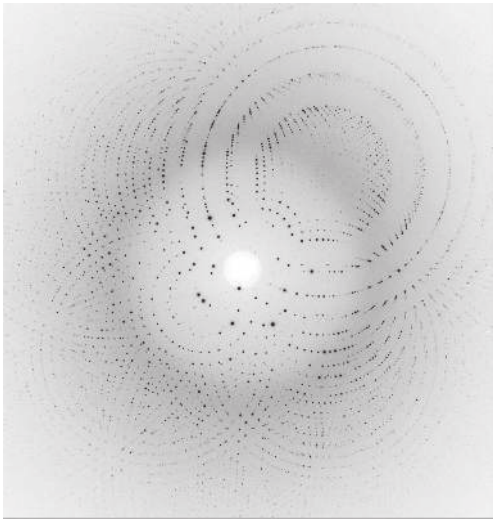

Fig. 4. A Laue diffraction image from a protein crystal collected on the MAR345 image plate detector at the APS 14-ID beamline.

when the mosaicity is increased. In most cases diffraction spots also become more elongated as a result of the photo-activation. In addition, the crystal will degrade as a result of radiation damage. The diffraction spots become more streaky and weaker, and the resolution to which crystal diffracts degrades during the experiment. The elongation of diffraction spots causes additional spatial overlap in the already crowded Laue diffraction images (**Fig. 4**) and spot integration becomes less accurate. Therefore, crystals need to be screened based on mosaicity and on the additional elongation of the diffraction spots when crystals are photo-activated. A compromise between the extent of photo-activation and the spot elongation often becomes necessary. The Laue processing software can handle successfully some degree of spot elongation (approx 4:1 ratio of spot length to spot width). However, one should keep in mind that the SNR is generally inversely proportional to the spot elongation for a given extent of photo-activation.

Crystal size consideration is very important. On the one hand, one needs large crystal volume to measure diffraction intensities with a sufficient SNR when using very short X-ray exposures. On the other hand, crystals cannot be too large as they will also become too optically thick at the wavelength used for reaction triggering (*see* **Subheadings 3.2.** and **3.4.**). In practice, this limits the thickness of the crystals in most cases to about 200 µm, unless special consideration is given to the geometry (*see* **Subheading 3.4.**).

Unlike standard diffraction experiments where crystals are routinely investigated at cryogenic temperatures (around 100 K), TR experiments probe structural changes at room temperature (around 293 K). Crystals are therefore more susceptible to radiation damage by X-rays. Crystals have to be mounted in thin-walled glass or quartz capillaries. Details on practical aspects of mounting crystals in capillaries can be found in the literature ***(30,31)***. Crystals should not be mounted too wet or too dry. A crystal embedded in too much liquid will move more easily when exposed to laser pulses, whereas a dry crystal will degrade faster because it will dry out further when repeatedly exposed to laser pulses. Crystals are typically maintained at a constant temperature by a dry gas stream. It is important to avoid temperature gradients across the capillary by using short capillaries and embedding the entire capillary into the gas stream. Otherwise, condensation or evaporation of the liquid at the crystal location may occur, which will degrade the crystal diffraction quality.

3.2. Reaction Triggering

A rapid and uniform reaction initiation, without a perturbing effect on the crystal or the reaction and with the highest possible fraction of activated molecules, is critical to the success of a TR experiment. Careful assessment and evaluation of the reaction initiation options is therefore essential. Depending on the nature of the reaction and reaction rates, triggering can be done by a rapid change in the concentration of substrates, cofactors, protons or electrons, by photo-activation of a native chromophore or a stable precursor of a substrate or cofactor, or by a rapid change in temperature or pressure.

The simplest method of concentration change is diffusion of substrates, cofactors or protons into a crystal in a flow cell. The method can be used to trigger a single reaction event ***(39–41)*** or a multiple turn-over, steady-state accumulation of an intermediate ***(42–44)***. However, the diffusion process is very slow ranging from seconds to many minutes ***(3,45)***, and only the slowest reactions can be triggered synchronously. These reactions can then be investigated either by Laue or monochromatic X-ray diffraction technique. Flash cooling following diffusion can also be instrumental in capturing the various stages of the reaction ***(39)***.

The fastest method for reaction triggering is photo-initiation using ultrashort laser pulses (fs to ns). Naturally suitable samples for this method are photosensitive proteins ***(13,16–23)***. Short laser pulses can also be used to induce a temperature jump in the crystal for studies of the initial steps of thermal unfolding in proteins ***(46,47)***.

For proteins that do not contain a chromophore and are not inherently photosensitive, phototriggering can be used in combination with caged or photolabile compounds. Caged compounds are inert precursors of substrate or

cofactor molecules. Illumination with UV light can liberate the active molecule and trigger the reaction in the crystal ***(45,48,49)***. A number of reactions have been triggered successfully on the μs to ms time scale using caged compounds ***(50–53)***. Very efficient and fast (sub-μs) caging groups are available now that can be incorporated into the hydroxyl, carboxyl, phosphoryl, and amide groups of a wide range of compounds. The compounds exist for photorelease of caged nucleotides, divalent cations (like magnesium and calcium), protons, neurotransmitters, and several amino acids.

Several concerns need to be addressed regarding the photo-initiation. The optical densities of photo-active crystals are often very high. The front layer of the crystal can therefore be easily over-saturated by light whereas the inner part of the crystal remains underexposed. For this reason, the wavelength of the laser light has to be selected such that the optical density is low (<0.5). This typically means that the wavelength is not at the absorption maximum, but on rather weak tails of the absorption bands. Another method to trigger the reaction more uniformly throughout the crystal is to illuminate the crystal from multiple sides.

It is beneficial if the optical density at the excitation wavelength is not only low for the initial state, but also for the intermediate state that forms during the laser pulse. Similarly, the use of shorter laser pulses will prevent the absorption of light by intermediates that form past the laser pulse duration. In both cases, the heating of the crystal will be reduced and a possible undesired photoactivation of the intermediate states is minimized.

The laser pulse energy delivered to the crystal has to be considered carefully. Too low energy will prevent sufficient photo-initiation, whereas too high energy may be damaging. Given the large number of molecules in the crystal (10^{12}–10^{14}), 10–100 μJ/pulse is needed just to match the number of absorbed photons to the number of molecules, assuming all delivered photons are absorbed. Because a relatively low optical density of the crystal is needed for a uniform photo-initiation, a significant fraction of photons will not be absorbed. Also, the laser beam size is typically larger than the crystal for easier alignment and overlap of the X-ray and laser beams (**Subheading 3.4.**), and to ensure a uniform reaction initiation across the crystal. This again reduces the number of photons that are actually absorbed and utilized for reaction initiation and requires higher pulse energy to be delivered. For example, for a crystal of $0.3 \times 0.3 \times 0.2$ mm^3 size containing 10^{14} molecules, with 0.2 OD at the excitation wavelength and the laser beam size of 0.6 mm diameter, only about 10% of the laser energy will be absorbed. As a result, about 1 mJ/pulse, rather than 100 μJ /pulse, has to be delivered to match the number of absorbed photons and number of molecules in the crystal. The temperature increase in the crystal due to the absorbed light is estimated to 1–2 K in this case. The quan-

tum yield (the number of reaction events per photon absorbed) also needs to be taken into account when determining the appropriate laser pulse energy. Other aspects of maximizing the reaction initiation in practice are discussed in **Subheading 3.4.**

When using caged compounds, similar considerations to those mentioned previously regarding the laser wavelength, pulse energy, and illumination apply. Caged compounds typically require intense UV light for activation ***(49)***, and crystal damage is a concern. For more efficient activation of caged compounds with low quantum efficiency, cryophotolysis has been proposed ***(4)*** in combination with temperature-controlled crystallography (rapid warm up/cool down cycle) to trap intermediates.

Preliminary spectroscopic measurements in crystals proved to be a very useful tool to characterize the purity of the sample, to monitor the extent of reaction initiation while optimizing the laser pulse energy, and to monitor the reaction progress in the chromophore region as a guide to TR crystallographic measurements. Several compact microspectrophotometers for on-line or off-line use have been described ***(54–57)***. The Hadfield-Hajdu design ***(55)*** is commercially available (www.4Dx.se).

3.3. Experimental Setup

3.3.1. X-Ray Source

Successful ns TR experiments have been conducted at two beamlines: ID09, ESRF and 14-ID, APS ***(16–18,20,22,28,58)***. The first sub-ns experiment (150 ps time resolution), conducted at the ID09 beamline, has been reported recently ***(13)***. Slower, µs to ms, experiments have also been conducted at the beamlines X26C (National Synchrotron Light Source, Brookhaven National Laboratory) and BL44B2 and BL40XU (SPring8).

At a synchrotron X-ray source, electrons emitted by an electron gun are first accelerated in a linear accelerator (linac), and then in a cycling booster synchrotron to their final energy of several GeV (7GeV at the APS). These high-energy electrons are injected into a large storage ring (1104 m circumference at the APS) where they orbit at a constant energy inside a vacuum chamber for many hours. Their revolution time is 3.683 µs at the APS storage ring. The electrons are bunched in the storage ring and produce intense X-ray pulses of approx 100 ps duration when passing through the bending magnets or insertion devices located around the storage ring ***(14)***. Insertion devices are arrays of magnets that force the electrons to follow a wavy trajectory, which results in more intense X-ray radiation than that produced by bending magnets.

Storage rings are typically operated with a uniform distribution of the electron bunches and thus produce a train of uniformly and quite closely spaced X-ray pulses. Standard operating modes at the APS are 324 or 24 uniformly

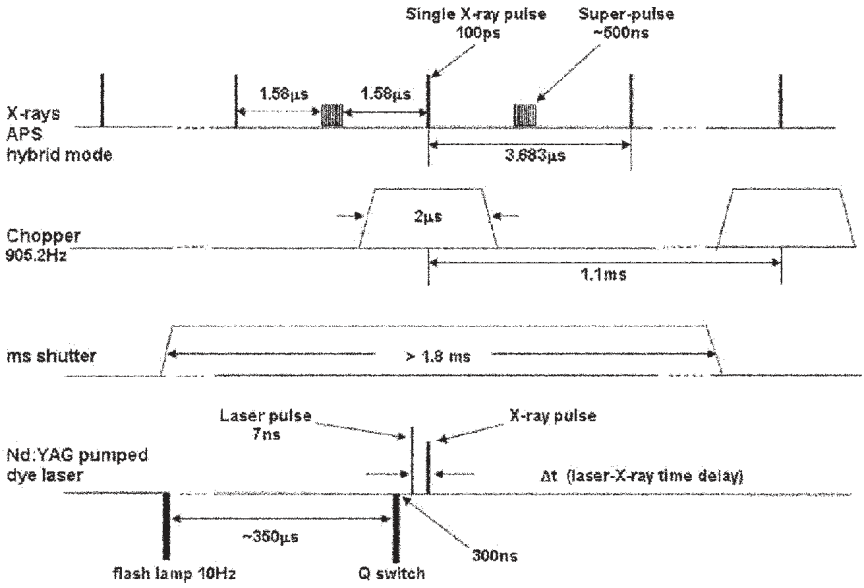

Fig. 5. Timing schematics for TR experiments at the 14-ID beamline, APS. Two X-ray shutters operate in series, synchronized to the X-ray pulse train, to select an X-ray pulse or a short pulse train. Laser firing is also synchronized with the X-ray pulses.

spaced single bunches (11.4 ns and 153 ns bunch spacing, respectively). X-ray shutters are used to isolate single X-ray pulses or super-pulses (trains of single 100 ps X-ray pulses with µs-ms duration). The fastest X-ray shutters ***(59,60)*** have open-time of 1–2 µs and can isolate a single X-ray pulse if the adjacent pulses are separated by more than 0.5–1 µs. This is the case in special operating modes of storage rings, such as the single bunch mode (ESRF) or the hybrid mode (ESRF and APS). In the single bunch mode only one electron bunch is circulating in the storage ring (2.816 µs spacing between consecutive X-ray pulses at the ESRF). In the APS hybrid mode, a single bunch is on one side of the ring while a train of closely spaced bunches (super-bunch) is located on the opposite side. The spacing between the single X-ray pulse and the adjacent super-pulse is 1.58 µs at the APS (**Fig. 5**).

At the polychromatic undulator beamlines of the third generation synchrotron sources, 10^9–10^{10} photons are delivered to a 200×200 µm^2 sample in a single X-ray pulse. This is, however, not sufficient to record a diffraction image with a SNR that is required to accurately determine small difference SF amplitudes. Signal averaging is required and 10–100 single X-ray pulse exposures are typically accumulated prior to the detector readout for each diffraction image (*see* **Subheading 3.4.**).

3.3.2. Synchronization and Timing of Laser and X-Ray Pulses

We will describe here the current experimental set-up at the APS beamline 14-ID, built and operated by the Consortium for Advanced Radiation Sources, The University of Chicago, Chicago, IL. For a detailed description of the ESRF beamline ID09 *see* Schotte et al. ***(60)***.

A series of shutters is used to select a single X-ray pulse from the continuous stream of pulses (**Fig. 5**). The fast rotating µs shutter (chopper) has a maximum rotation frequency of 905.2 Hz and a minimum open-time of 2 µs (FWHM). The phase of the chopper relative to the X-ray pulse train is adjustable so that the chopper can transmit either a single, 100 ps X-ray pulse or a 500 ns super-pulse in the APS hybrid mode. The slower ms shutter, with a minimum open-time of 1.8 ms (FWHM), isolates a single opening of the chopper. Two additional, even slower shutters (so-called *heat-load* shutters) are used to prevent excessive heating of the chopper by polychromatic radiation.

Two tunable ns lasers are available for reaction photo-initiation: a Nd:YAG pumped dye laser (Continuum Powerlite 8010/ND6000) and a more easily tunable Nd:YAG pumped OPO laser (Opotek Vibrant). The pulse duration for the two lasers is 7 ns and 4 ns, respectively. The wavelength range accessible with these lasers is 420–850 nm and 240–620 nm, respectively. A timing module (in-house design) provides synchronization of the laser and X-ray pulses. The actual synchrotron RF signal is used as a synchronizing *clock* for both the timing module and the chopper controller. The timing module generates a 10 Hz signal for necessary continuous operation of the Nd:YAG laser flash lamps and also provides the trigger for laser firing. Both signals are sent to the laser via a very accurate time-delay generator (Stanford Research DG535) that facilitates adjustment of the time delay between the laser and X-ray pulses in the range from 1 ns to many seconds.

3.3.3. Sample Environment

The ns lasers are located in the remote laser laboratory. Laser light is passed to the X-ray station and delivered to the sample via an optical fiber. Fibers with a relatively large diameter are used (0.6–0.9 mm) because the laser pulse energy of a few mJ (*see* **Subheading 3.2.**) has to be coupled into the fiber. The coupling is accomplished by focusing the laser light at the tip of the fiber, while exposing only the fiberglass core to the light to prevent damage of the fiber.

The standard arrangement of components in the sample area is shown in **Fig. 6**. The laser beam is focused onto the sample by a small collimating/focusing assembly (L) that provides approx 1:1 focusing. Another optical fiber (not shown) is mounted opposite to the shown fiber for a more efficient reaction photo-initiation (*see* **Subheadings 3.2.** and **3.4.**). The optical paths are adjusted so that the light from both fibers reaches the sample simultaneously (± 0.5 ns).

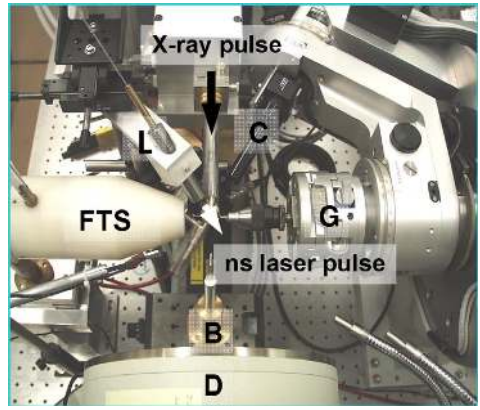

Fig. 6. Sample environment at the 14-ID beamline, APS. The sample capillary is mounted on the goniometer head (G) of a standard kappa diffractometer. The camera for viewing the magnified image of the crystal (C) is also mounted on the diffractometer. The sample is maintained at a constant temperature by a gas stream from the cooling system (FTS). The X-ray beam stop (B) and the MARCCD area detector (D) are also shown.

Two avalanche photodiodes are used to detect the laser and X-ray pulses separately as signal strengths vary significantly. Both are located very close to the sample (not indicated in **Fig. 6**). A diode with a Be window is used to detect the X-ray pulses only. The second diode detects predominantly laser pulses (much stronger signal). The time-offset between the two diodes is fixed and known. The signal from these diodes is sent to a fast oscilloscope (500 MHz Tektronix TDS744A) for measurement of the time delay between the pulses.

3.4. X-Ray Data Collection

3.4.1. Reaction Triggering Considerations

A general scheme of TR X-ray data collection can be described as follows. A single laser pulse is directed to the desired volume of the protein crystal and after a well defined time delay a single X-ray pulse illuminates the laser-irradiated volume. The diffracted X-rays are recorded on a large area detector. Because the signal of interest is the difference between the diffraction before and after the photo-activation, the alignment of the crystal, the X-ray beam, and the laser beam is critical. First, the center of rotation of the diffractometer is brought into the X-ray beam path. The laser beam is then focused at the center of rotation. Finally, the crystal is placed at the center of rotation. The crystal therefore stays at the same position during the data collection, at the intersection of the laser and X-ray beams.

As mentioned in **Subheading 3.3.**, even the most powerful, third-generation synchrotron sources require multiple pump-probe cycles for ns or sub-ns time resolution. Between each pump-probe cycle there must be a wait-time for the original state to be restored in the crystal. The wait-time depends on the cycling time of the sample and the time needed to dissipate the heat deposited by the laser pulse. If the wait-time is too short, the heat may not dissipate before the next pump-probe cycle and the temperature of the sample might creep up with repeated pump-probe cycles. For this reason, the repetition rate is usually only a few Hz even when the cycling time of the protein is faster.

When a crystal is exposed to laser pulses, the increase in crystal mosaicity and crystal motion are generally observed and manifested as elongation (streakiness) of the diffraction spots. The increase in mosaicity can be observed even with a single X-ray pulse exposure whereas the crystal motion is most clearly evident with multiple exposures. The main cause for the crystal motion is thought to be heating related. To reduce the motion, a sufficient wait-time between cycles, as well as minimizing the number of pump-probe cycles should be considered. Also, immobilizing the crystal inside the capillary is highly beneficial. This has recently been successfully accomplished for a variety of crystals by using either glue (standard 5-min epoxy, for example) or a thin coat of polyvinyl to attach the crystal to the capillary ***(61)***.

The X-ray exposure should be maximized without compromising the time resolution for a given time delay. Whenever possible, a train of X-ray pulses should be used for the pump-probe cycle rather than a single X-ray pulse, because more X-ray photons are used per cycle and an image can be obtained with a smaller number of cycles. This has two advantages. First, the total time for the experiment is reduced. Second, the number of laser shots and therefore the crystal damage by the laser pulses is reduced.

The spatial extent of structural changes as well as the overall fraction of photo-activated molecules is generally small. It is therefore imperative to maximize the signal and minimize the background. The SNR of the difference signal is roughly proportional to the square root of the total number of X-ray photons and to the overall fraction of photo-activated molecules, which in turn is proportional to the absorbed energy of the laser pulse (other conditions being equal). Therefore, laser beam size and X-ray beam size should be adjusted to maximize the fraction of excited molecules probed by the X-ray beam. The size of the X-ray beam is the same or slightly smaller than the size of the crystal in order to optimize the SNR. If the X-ray beam is larger than the crystal, the background from the capillary and the liquid around the crystal is increased. On the other hand, if the X-ray beam is too small, a part of the crystal will not contribute to the diffraction. The X-ray beam is typically smaller than the laser beam as the laser beam is generally larger than the crystal (*see* **Subheading 3.2.**).

Larger crystals are preferred because they result in better diffraction, and therefore better difference signal. Efficient photo-activation, however, becomes a problem if the wavelength cannot be tuned to a region where the optical density is sufficiently low (*see* **Subheading 3.2.**). In cases where optically thick crystals have to be used, a small X-ray beam can be used to probe only the surface layer of the crystal that is illuminated by laser light. It is important that the surface layer stays at the intersection of the laser and X-ray beams for all crystal orientations during the data collection.

To minimize systematic errors, ideally all time delays should be collected using a single crystal. In practice, however, this is often not possible because of crystal damage by the X-ray and laser pulses. This limits the maximum number of images that can be collected from one crystal (*see* **Subheading 3.4.3.**). When crystal morphology allows, using long but relatively thin crystals with smaller laser and X-ray beams can be beneficial. The crystal can be translated and the previously unexposed part of the crystal can be used for subsequent data collection.

The laser pulse energy has to be optimized to maximize the photo-activation while preventing the crystal damage and excessive spot elongation (*see* **Subheading 3.1.**). Typical pulse energies are of the order of several mJ for the laser beam size of 0.6–0.9 mm (diameter). When a time series of data sets is collected, the laser pulse energy should be held constant for all time delays. A failure in this regard will introduce systematic errors as the extent of photo-activation will differ for different time delays.

3.4.2. X-Ray Beam Considerations

Undulators, that have an energy bandpass significantly narrower than wigglers, proved to be better X-ray sources for Laue and TR crystallography ***(15,62,63)***. In addition to the reduced polychromatic background and spatial overlap in the Laue images, the higher peak power of undulators also contributes to the improved data quality. The APS Undulator A, used on the 14-ID beamline, has an energy bandpass of approx 1 keV ($\Delta E/E \sim 10\%$, FWHM), compared to the bandpass of approx 10 keV of the APS Wiggler A.

X-ray wavelength and flux are determined by the undulator gap. The Undulator A at 14-ID beamline is typically operated with the energy of the first harmonic in the range of 11.3 to 13.8 keV (0.9 to 1.1Å). Because it is critical that the X-ray flux is maximized for TR experiments, the choice of the wavelength is only the secondary factor. It should be noted, however, that shorter wavelengths cause less radiation damage ***(64)*** and this can therefore be important for room temperature studies.

3.4.3. Data Collection Strategies

In TR Laue crystallography, a complete data set is a multidimensional data matrix: three traditional reciprocal space dimensions and the additional dimen-

sion of time. At a particular crystal orientation and time delay, the Laue diffraction pattern contains diffraction spots only for a part of the reciprocal space. Laue images at many different crystal orientations have to be collected to completely sample the reciprocal space at each time delay. The angular step through the reciprocal space depends on the bandpass of the X-ray source. With the APS Undulator A, 2–3° is sufficient. The number of time-points needed and their distribution in time ultimately depends on the reaction that is investigated but a good starting point is to collect three to five points per time decade in the region of interest, equally spaced in logarithmic time.

The beamtime is quite limited at synchrotrons in general. In addition, the special operating modes required for TR experiments are available for only a very limited amount of time. Therefore, one should make a considerable effort to use beamtime efficiently. The mode of experiments and data collection strategy depends on the goal of the experiment. If crystals are being checked for suitability for TR Laue experiments, snapshot images are collected without the laser excitation to evaluate the crystal mosaicity. If the suitability has already been established and real TR data is to be obtained, one often faces two possibilities depending on the choice of the fast variable: crystal orientation or time delay. The most straightforward data collection scheme is to scan the entire angular range at a fixed time delay and subsequently move to another time delay. Because only a limited number of images can be obtained from one crystal as a result of radiation damage, only single time-point or at most a few time-points can be obtained from one crystal. Therefore, in this experimental scheme, laser intensity fluctuation and crystal-to-crystal variation between time-points introduce a systematic error that has a detrimental effect on the accurate determination of the time constants when the entire series of time delays is examined. Nevertheless, this collection strategy is often chosen if the goal of the experiment is to collect preliminary data at a few chosen time delays in order to establish the presence of the signal and determine the photo-activated fraction of molecules. In addition, a highly redundant data at a desired time delay can be obtained most effectively this way by merging multiple data sets collected at the same time delay ***(58)***.

The problem of systematic errors described previously can be circumvented by an alternative data collection scheme where the time delay, rather than the angular setting, is the fast variable. The time range is scanned at a fixed angular setting, which is then advanced for a repeated time scan at the new crystal orientation. A shortcoming of this method is that one crystal may not be sufficient to obtain data for all crystal orientations and all time delays as a result of radiation damage issues. Fortunately, our experience suggests that data from multiple crystals can be merged successfully. Therefore, data sets that are partial in reciprocal space but which cover all time delays can be collected from

several crystals and merged to obtain a time series of complete data sets. This constitutes a better method for accurate determination of time constants associated with the formation and decay of intermediates.

Another shortcoming of this approach of data collection is the potential all or nothing aspect. If the entire reciprocal space for the series of time delays is not completed, the data may turn out to be useless. One may run out of beamtime or crystals. This becomes a more serious problem with lower X-ray flux and space groups with low symmetry like monoclinic, where an angular range of 180° has to be collected. To minimize the risks but complete the entire time series that is needed, one can collect several shorter time series rather than one long series. In this case, one time delay common to all time series is desirable as it will greatly help to account for any variation in the extent of photoactivation among different time series.

Because the actual signal in the TR data is the change caused by the reaction initiation, a reference data should be collected and subtracted from the data at positive time delays (so-called light data). It may be possible to use a model from a static measurement as a reference without collecting experimental reference data. However, our experience shows that an experimental reference data collected without light activation (so-called dark data) is superior in reducing systematic error and yield a better SNR. The best way to minimize the systematic errors is to interleave dark and light images for single-time delay if crystal orientation is the fast variable, and to collect dark plus light time series if time delay is the fast variable. This way, any progressive degradation of the crystal will have a minimal effect in the final difference signal. In addition, a negative time delay instead of dark data can be used as a reference. This has an advantage of reducing any systematic error due to potential accumulation of photoproducts during the data acquisition.

3.5. Data Processing and Analysis

Processing of TR data proceeds in three steps: 1) a time series of structure factor amplitudes is derived from diffraction images; 2) a time series of difference electron density maps is derived; and 3) structures of intermediate states are determined. The three steps are explained in **Subheadings 3.5.1.** to **3.5.9.**

3.5.1. Reducing Laue Data

The goal of data reduction is the extraction of accurate diffraction spot intensities or SF amplitudes from the raw images (**Fig. 4**). The major steps involved are indexing, integration, scaling, and deconvolution of harmonic overlaps ***(15)***. The first three steps are challenging for the polychromatic, Laue method, whereas the fourth step is actually unique for this method. Specialized

software is used for processing of Laue data (*see* **Subheading 2.**). The software must cope with the following problems specific for the Laue method:

1. In crowded Laue diffraction patterns probability is high that the reflections spatially overlap. Spot profiles are used to separate these overlaps ***(32,37)***. The profiles are derived from well separated, nonoverlapping reflections. By using the narrow bandpass undulators as X-ray sources, the spatial overlap problem is significantly reduced ***(62,63)***.
2. The intensity of the polychromatic incident radiation varies as a function of wavelength. In addition, the scattering power of the crystal as well as other parameters such as the detector sensitivity are wavelength dependent ***(26)***. When the orientation of the crystal is changed, a given reflection may be stimulated at a different wavelength. Consequently, intensity collected from this reflection or its symmetry mates may vary strongly with the orientation of the crystal. Therefore, the intensities must be brought to a common scale before they can be merged. This procedure is known as wavelength normalization and results in a so-called λ-curve, which represents all wavelength dependent effects as seen by the detector ***(32,35)***.
3. The polychromatic X-ray beam may excite at the same time reflections whose indices are multiples of a common basic hkl triplet. For example, the reflections with indices 2 4 0 and 3 6 0 both contain a multiple of the basic 1 2 0 triplet and are, therefore, harmonic to each other. Harmonic reflections lie on a radial line in the reciprocal space (starting at the origin), scatter in exactly the same direction and overlap precisely at the detector ***(33)***. As these reflections correspond to different energies, the overlap is also referred to as energy overlap. The low-resolution reflections are especially affected, leaving the low-resolution data incomplete (*low resolution hole*) if the harmonic overlaps are excluded. Using multiple measurements of the same reflection at different crystal orientations and measurements of corresponding symmetry mates, the harmonic overlaps can be resolved into the component reflections after the λ-curve has been determined. The procedure is referred to as harmonic deconvolution.

Laue data reduction is also affected by a substantial scattering background generated by the polychromatic radiation. As a consequence, weak reflections that occur predominantly at higher resolution are more difficult to determine accurately than for the monochromatic data. The background is substantially reduced by use of undulators (*see* **Subheading 3.3.1.**) which improves the overall resolution of the collected data.

3.5.2. Time-Dependent Difference Electron Density Maps

The result of a TR experiment are SF amplitudes of the initial, dark state $|\mathbf{F^D}(hkl)|$ and a corresponding set of time-dependent SF amplitudes $|\mathbf{F}(hkl,t)|$. From these amplitudes, time-dependent difference SF amplitudes $\Delta F(hkl,t) = |\mathbf{F}(hkl,t)|-|\mathbf{F^D}(hkl)|$ are calculated for each time-point t. Phases ϕ^D_{hkl} are obtained from the known dark state structural model. If both $|\mathbf{F}(hkl,t)|$ and $|\mathbf{F^D}(hkl)|$ are on the absolute scale, it can be shown ***(65,66)*** that DED maps calculated using

$\Delta F(hkl,t)$ and the phases ϕ^D_{hkl} are accurate maps on roughly half the absolute scale as long as structural differences remain small and noise moderate. This is referred to as the difference approximation. However, significant random noise in the difference SF amplitudes $\Delta F(hkl,t)$ will have a degrading effect on the maps ***(27,66)***. Moreover, as a result of errors in data acquisition and reduction some $\Delta F(hkl,t)$ may be erroneously large. Consequently, both, extremely large $\Delta F(hkl,t)$ and those with a high experimental error should be weighted down in calculations of DED maps. Several weighting schemes have been proposed ***(16,20,27,67)***. The final DED map is calculated as:

$$\Delta\rho(t) = \frac{1}{V_e}\sum_{hkl} w\Delta F(hkl,t)e^{i\phi^D_{hkl}}e^{-2\pi i(hX+kY+lZ)} \quad (2)$$

where *X, Y, Z* are the components of the position vector in the coordinate system of the unit cell (fractional coordinates), *h, k, l* are the reflection indices, V_e is the volume of the unit cell and *w* is the weighting factor of the difference SF amplitude $\Delta F(hkl,t)$.

These maps can be inspected using specialized molecular modeling programs such as XtalView ***(68)*** or O ***(69)***. In order to display the features that are above the noise of the map, the DED maps need to be contoured above the 3 σ level. The σ value is the root mean square (RMS) deviation of the DED from the mean value determined from all grid points in the asymmetric unit. It includes contributions from both signal and noise. Positive and negative DED features are observed. Negative electron density features represent loss of electrons and account for atoms that have moved away. Positive features represent gain of electrons and account for new positions occupied by atoms that moved. If SF amplitudes are represented on the absolute scale and nonoverlapping DED features are considered, the total (integrated) DED count in a particular feature multiplied with the volume of the grid unit is equivalent to about half the number of electrons displaced from or into this volume.

3.5.3. Structures of the Intermediates and Chemical Kinetic Mechanism From Difference Electron Density Maps

The ultimate goal of any TR experiment is the determination of the kinetic mechanism together with the atomic structures of the underlying intermediates (*see* **Subheading 1.**). Chemical kinetics is the key to analyze the experimental DED maps, to separate admixtures of intermediates present in these maps, and to determine the structures of the intermediates.

The kinetic analysis starts with the search for the number of intermediates and determination of relaxation times (*see* **Subheading 1.**) by examining the series of time-dependent, experimental DED maps. How to find the number of relaxation times from the series of DED maps represented by a large number of grid points which can amount to 10^5 even in moderately sized DED maps?

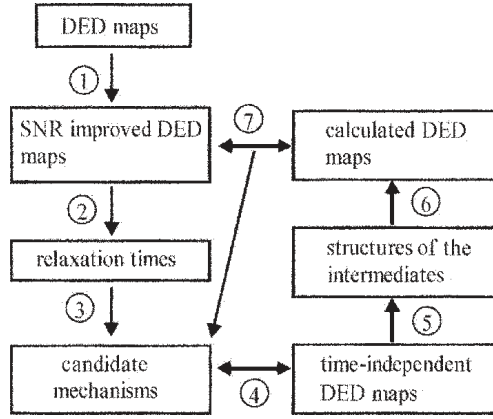

Fig. 7. The seven steps from the time-dependent DED maps to the structures of intermediates and compatible kinetic mechanisms. 1) Noise reduction via SVD-flattening of the DED maps. 2) Fit of the right singular vectors, the main temporal components of the experimental maps derived by SVD, by exponential functions. 3) Fit of candidate reaction mechanisms to the right singular vectors. 4) Construction of the time-independent DED maps corresponding to intermediates from left singular vectors (major spatial components derived by SVD). 5) Extrapolated, conventional electron density maps of the intermediates and modeling of intermediate structures. 6) Calculation of time-dependent DED maps from structures of intermediates for chosen candidate mechanisms. 7) Comparison of calculated and observed time-dependent DED maps on the absolute scale, post-refinement and selection of candidate mechanisms by a *posterior analysis*.

Tools are available from linear algebra, which perform just this task. These tools are all related to a component analysis. One of the tools, the Singular Value Decomposition (SVD), has been shown to work successfully with crystallographic data ***(27–29)***. The SVD separates time and space variables: from a series of time-dependent difference maps it determines only a few main common spatial components and their time variations, which constitute main common temporal components. The temporal components are then used to determine the number of intermediate states and relaxation times.

Figure 7 shows schematically the main steps in the process of deriving the time-independent maps of the intermediate states from the measured, time-dependent DED maps. Before we assess the main features of each step, the application of SVD to the crystallographic data is explained.

3.5.4. Singular Value Decomposition in Time-Resolved Crystallography

To perform an SVD analysis, a data matrix ***A*** is prepared where the difference maps from a time-series are entered one by one and in temporal order as

column vectors of the matrix. How the grid points of the DED maps are assigned to the elements of the column vectors of $\boldsymbol{A}$ is irrelevant. However, a chosen order must be consistently used for all maps. If crystallographic symmetry is present, only the asymmetric unit needs to be included. Even more, a mask can be used to consider only the volume occupied by protein atoms. Around $M = 10^5$ grid points per map have to be considered for a protein of 20 kD molecular mass. A further reduction in the number of considered grid points is possible if those that do not contain significant difference electron densities throughout the time-course are disregarded. For this purpose a grid point is included only if DED is above or below a chosen σ level for at least one time point (typically the $\pm$ 2 σ level). Thus, the number of useful grid points can be reduced to around $2 \cdot 10^4$ for the mentioned small protein.

An $M \times N$ data matrix $\boldsymbol{A}$ composed of DED maps at N time points, each consisting of M grid points, is decomposed into an $M \times N$ dimensional matrix $\boldsymbol{U}$, which contains the left singular vectors (lSV), an $N \times N$ square diagonal matrix $\boldsymbol{S}$, diagonal elements of which are the singular values (SV) and the transpose of a $N \times N$ square matrix $\boldsymbol{V}$:

$$A = \boldsymbol{USV}^{\boldsymbol{T}} \tag{3}$$

The rows of $\boldsymbol{V}^{\mathrm{T}}$ are the right singular vectors (rSV). The lSV are the main spatial components of the experimental, time-dependent DED maps and are DED maps themselves. Each rSV contains the temporal variation of the corresponding lSV DED map, whereas the SV weights the contribution of the lSV map to the experimental DED maps.

Although N singular vectors result from the SVD decomposition, not all of them contain signal. To those that do, we refer to as significant. The number of significant singular values and vectors is related to the number of intermediates in the reaction. Consider a reaction where molecules initially in the state I_0, when photo-excited, go through two sequential intermediate states, I_1 and I_2, and back to the initial state, $I_1 \rightarrow I_2 \rightarrow I_0$. In this hypothetical experiment, time-dependent DED maps are collected at N = 10 time delays. In this case, only two difference maps are present, I_1–I_0 and I_2–I_0, corresponding to two intermediates. All measured DED maps are a mixture of various ratios of these two difference maps. After the SVD, there are only two significant lSV. The first significant lSV_1 represents the average DED map of the relaxation processes and the rSV_1 describes its temporal variation. Consequently, the lSV_1 is a mixture (a linear combination) of the I_1–I_0 and I_2–I_0 difference maps. The second significant lSV_2 is also a linear combination of the I_1–I_0 and I_2–I_0 maps. It has a lower SV and contains the average deviation from the average difference map lSV_1. The second rSV_2 describes its temporal variation. The lSV_1 and lSV_2 maps occupy the first two columns in the $\boldsymbol{U}$ matrix while the rSV_1 and rSV_2 occupy the first two rows of the matrix $\boldsymbol{V}^{T}$, since the singular vectors

and values are ordered according to the magnitude of the singular values, i.e., according to their significance. The remaining eight vectors at positions 3 to 10 in the matrices ***U*** and ***V*** are insignificant and contain only noise.

It is straightforward to expand these considerations to more intermediate states. In general, if the number of time-points is larger than the number of intermediate states, the data matrix ***A*** can be approximated by a matrix ***A'*** reconstructed from a small number S of significant singular vectors containing signal. There is an inherent SNR improving capability in the SVD analysis as reconstructing the data matrix from the significant singular vectors in effect filters the noise out. When substantial noise is present, the signal will artificially spread to insignificant singular vectors. In this case, the procedure of rotation can be used to recollect the signal ***(28,29,70)***. The SVD noise-filtering is still effective.

3.5.5. ***Step 1:*** *Noise Filtering (Singular Value Decomposition Flattening)*

The experimental noise results in errors in magnitude and, more importantly, sign of the difference SF amplitudes (negative sign instead of positive or vice versa). This gives rise to DED features varying randomly in time ***(28,66)***. The SVD can correct for these errors. However, it is crucial that the number of significant singular vectors, containing signal, is determined correctly. All vectors containing the signal have to be used to reconstruct the approximate data matrix ***A'*** . The methods for selecting the significant vectors ***(27–29)*** are based on the magnitude of the singular value and on the autocorrelation of the rSV, but, most importantly, on identifying the regions of the molecule where signal is present by inspecting the DED maps represented by the lSV (**Fig. 8**).

From the DED maps reconstructed using only significant singular vectors and values, new difference SF amplitudes and phases, $\Delta F^{SVD'}$ and $\phi^{SVD'}$, are obtained by an inverse Fourier transform. These difference SF are combined with the SF for the dark (initial) state by a phase recombination scheme ***(27,28)***, to result in improved values ΔF^{SVD} and ϕ^{SVD} and, from these, to DED maps $\Delta\rho(t)^{SVD}$ with improved SNR. It has been shown with the mock data ***(27)*** that the initial dark phases used for the difference SF can be improved by this procedure by 10°–15°, depending on the noise. In other words, the initial dark phases approached by 10°–15° to the true phases of the difference SF. In mock and experimental difference maps the SNR is greatly enhanced ***(27–29)*** and the maps are much better suited for a subsequent kinetic analysis. This new procedure for noise suppression has been named SVD-flattening. **Figure 9** shows an experimental DED map before and after the SVD-flattening is applied to a time series of 15 experimental DED maps (drawing produced by Ribbons ***[71]***). It is clearly demonstrated that for the flattened maps (panel B), the signal is enhanced and the noise reduced.

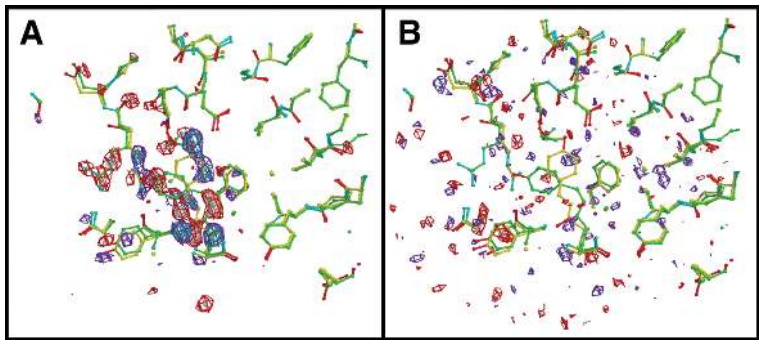

Fig. 8. **(A)** Significant left singular vector **(B)** Insignificant left singular vector. (Both from mock data.)

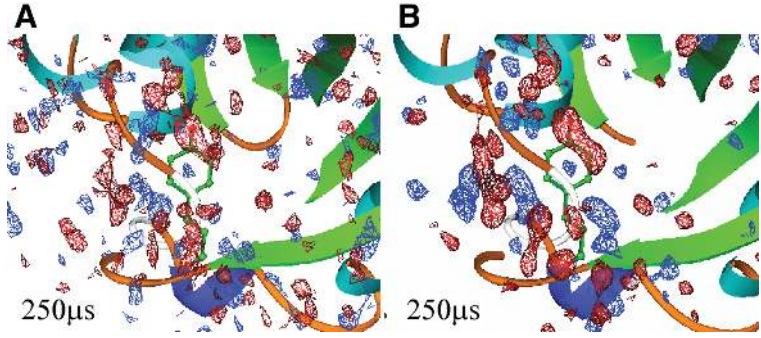

Fig. 9. DED map at 250 µs from a set of 15 experimental DED maps ***(28)*** **(A)** original DED map **(B)** SVD-flattened DED map, contour levels: red/white: –3 σ/–4 σ, blue/cyan: 3 σ /4 σ.

3.5.6. ***Step 2:*** *Relaxation Times*

The next step in the SVD analysis is to subject the SVD-flattened maps, $\Delta\rho\,(t)^{SVD}$, to the SVD procedure again. The resulting significant rSV are examined as they contain the temporal variations of significant lSV, the main spatial components. The rSV time-traces are linear combinations of the true time-dependent concentrations of intermediates. Hence, the rate coefficients λ_i and the corresponding relaxation times τ_i remain unchanged and can be determined from the rSV. All rSV are fit globally with a sum of exponential terms featuring common relaxation times τ_i (step 2 in **Fig. 7**). **Figure 10** shows the first four rSV from an analysis of real experimental data. Three relaxation times are identified at 170 µs, 620 µs, and 8.5 ms (marked by vertical lines).

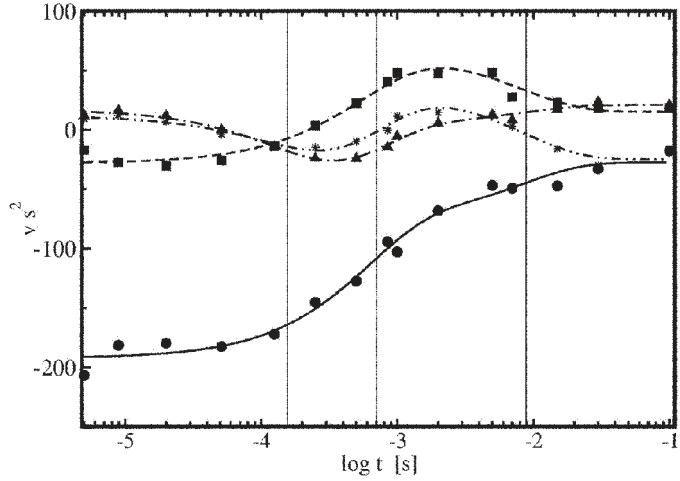

Fig. 10. rSV from a SVD analysis of experimental data ***(28).*** Vertical lines mark the identified relaxation times. Data points: ● first rSV, ■ second rSV, ▲ third rSV, * forth rSV. Fitted exponentials are shown for rSV1 to rSV4 by solid, dashed, dashed dotted, and dashed double dotted lines, respectively. Some signal has spread into the fourth rSV owing to noise ***(27)***.

3.5.7. ***Steps 3*** *and* ***4****: Time-Independent Difference Electron Density Maps*

This part of the SVD analysis is more complex, because here the DED maps corresponding to intermediates must be synthesized from the significant lSV. Although lSV are DED maps, they are only linear combinations of the DED of the intermediates. In order to determine the contribution of each significant lSV to the DED map for each intermediate, time-dependent concentrations of intermediates are needed. This requires the assumption of a mechanism. The mechanism must be compatible with the relaxation times observed in the rSV, i.e., it must generate both the correct number and the correct values of the relaxation times (**step 3** in **Fig. 7**). Because the number of relaxation times is related to the number of states, a general mechanism can be set up that contains all states and all possible rate coefficients between them (as in **Fig. 1**, panel G). For chosen plausible simple candidate mechanisms based on this general mechanism, the time-dependent concentrations of intermediates, I_j, are derived by solving a system of coupled differential equations for each mechanism (**Fig. 2**). The significant rSV are then fit again globally, this time by the sum of concentrations, I_j, with the scale factors E_{nj} as amplitudes for the n-th rSV and the j-th concentration term (*see* **Note 1**, **Eq. 4**). Concentrations are expressed in terms of rate coefficients (**Fig. 2**). Both the numerical values of the rate

coefficients and the scale factors E_{nj} are varied to reproduce (fit) the magnitude of all relaxation times in rSV (*see* **Note 1**, **Eq. 4**).

The resulting scale factors E_{nj} determine the contribution of the n-th lSV to the DED map of the j-th intermediate. The intermediate DED maps can now be synthesized (*see* **Note 1**, **Eq. 5**, and **step 4** in **Fig. 7**). The mixture of intermediates in the experimental time-dependent DED maps has therefore been separated into the time-independent DED maps of intermediates. An example is shown in **Fig. 11**, panel A ***(28)***. Most of the red, negative DED features are located on dark state atoms (green) whereas the blue, positive DED features can be interpreted by an atomic model of a single intermediate.

3.5.8. ***Step 5:*** Structures of the Intermediates

DED maps are difficult to interpret. Density is often disconnected, positive and negative densities are not always paired, and positive and negative densities can overlap as molecular rearrangements occur, leaving no density at the overlap locations. The interpretation difficulties can be overcome using conventional electron density maps calculated from the so-called extrapolated structure factors. These SF are obtained by a vector summation of the calculated SF of the dark state and the difference SF resulting from the Fourier transform of the time-independent DED map of an intermediate determined in **step 4** (*see* **Note 2**, **Eq. 6**). The amplitude of the difference SF is extended to correspond to 100% photo-initiation. As a result, each of these conventional electron density maps represents one pure intermediate only (no contribution from the dark state). The structures of intermediates can therefore be modeled and refined using these maps.

However, at this stage of the analysis, several candidate mechanisms can still extract similar, interpretable DED and conventional maps for intermediates, and cannot be distinguished. This is a general difficulty that arises when rSV are analyzed with a kinetic model. In the next paragraph a possible approach, named *posterior analysis*, is proposed to partially solve this problem.

3.5.9. ***Steps 6*** and ***7:*** Chemical Kinetic Mechanism: Calculated Time-Dependent DED Maps and Posterior Analysis

To compare different candidate mechanisms, one has to consider values for both relaxation rates λ_i and amplitudes P_{ji} in the expressions for concentrations of the intermediates I_j (**Fig. 2**) when fitting the rSV. Even when relaxation rates are very similar for different mechanisms, the amplitudes P_{ji} will be different, and it should be possible to use them to distinguish between these mechanisms. However, the rSV are not on the absolute and common scale, but rather on an arbitrary and unknown scale. As mentioned earlier, the scale factors E_{nj} are needed to bring the concentrations I_j (which are on the absolute scale) to the scale of the rSV. Therefore, the amplitudes P_{ji} cannot be used to

distinguish between the candidate mechanisms. However, once additional, chemical information such as the structural and stoichiometric constraints enter the analysis, a further discrimination becomes possible.

Stoichiometric constraints are automatically included when the observed SVD-flattened DED maps, $\Delta\rho(t)^{SVD}$, are presented on the absolute scale: DED is expressed in the absolute units of e/Å^3 and fractional contributions of atoms (occupancies) can be determined. The $\Delta\rho(t)^{SVD}$ can be used to distinguish between mechanisms and, even more importantly, to estimate the extent of reaction initiation. Given the models of the ground state and the intermediates, and a candidate kinetic mechanism, time and mechanism (k) dependent DED maps, $\Delta\rho(t,k)^{calc}$, are calculated (**step 6** in **Fig. 7** and **Note 3**, and **Eq. 7**). Initially, the extent of the reaction initiation is set to 1.0 and reasonable initial conditions are assumed, which determines the coefficients P_{ji}. The $\Delta\rho(t,k)^{calc}$ are compared (fit) at all time-points to the $\Delta\rho(t)^{SVD}$. The difference is initially large for all time-points as the reaction initiation has to be adjusted to the observed level. In subsequent steps the rate coefficients for the candidate mechanism are refined (*see* **Note 3**, **Eq. 8**).

After the fit has converged, the residual maps $\Delta\Delta\rho(t) = \Delta\rho(t)^{SVD} - \Delta\rho(t,k)^{calc}$ are inspected. If they are free of density for all time-points, the mechanism is considered compatible. It has generated concentrations that reproduced the observed difference electron density. However, if there is pronounced residual density $\Delta\Delta\rho(t)$ at some or all of the time-points the mechanism is considered inconsistent and should be disregarded. A new candidate is then tested (**Fig. 7**, **Step 7**). Usually, from a set of simple mechanisms in the general mechanism scheme for the given number of intermediates, only a few mechanisms prove to be incompatible and the remaining ones constitutes a set of possible kinetic mechanisms. The degeneracy of the problem is therefore diminished, but not removed.

3.6. Applications of Time-Resolved Crystallography

Several review articles have summarized the progress in studies of structural intermediates by TRX and by trapping methods on a number of proteins ***(1–3,15,25,72,73)***. For some proteins, a detailed characterization of intermediates on the reaction pathway has been obtained using either one or both approaches. Examples include: isocitrate dehydrogenase ***(42)***, hammerhead ribozyme ***(39)***, bacteriorhodopsin ***(8)***, cytochrome $P450_{cam}$ ***(74)***, horseradish peroxidase ***(75)***, myoglobin ***(13,16–18,76–80)***, and photoactive yellow protein ***(20–22,81)***. A comprehensive table of TR Laue diffraction experiments from 1986 to 1998, with a time resolution from 10 ns to several seconds, is given in **ref. *15***. We will summarize here the results for two proteins that have been studied with the best time resolution to date: myoglobin and photoactive yellow protein.

3.6.1. Myoglobin

This small, oxygen-binding heme protein (18 kD) has been extensively studied by numerous experimental techniques for many decades. It is the first protein for which a three-dimensional structure was determined by X-ray diffraction ***(82)***. As the structure revealed no open pathway for the ligand access to the heme, the importance of protein dynamics for the process of ligand binding became evident. Since then, numerous studies of myoglobin established it as a model system to understand the complex nature of protein dynamics and protein–ligand interactions. The cabonmonoxy complex of myoglobin (MbCO), as very stable and easily photolyzed, is particularly well-suited for TRX studies. The goals of these studies are to elucidate the structural basis of the photolysis-induced protein relaxation processes ***(10,11)*** and the nature of the *proteinquake* ***(83)***, as well as to determine the pathway of the photodissociated ligand through the protein matrix.

The ns and sub-ns TR room temperature studies of myoglobin ***(13,16–18)*** demonstrate the capability of the technique. Myoglobin is a challenging case for TRX studies because structural changes following ligand photodissociation are expected to be small (0.2–0.4Å), based on high-resolution, static structures of MbCO and deoxy forms of myoglobin ***(84)***. Nevertheless, such small changes have been detected and the photodissociated CO molecule (CO*) has been identified on its migration pathway through the protein, even at relatively low occupancy levels of 10 to 20%.

In the first ns TR experiment ***(18)*** data sets to 1.8 Å resolution were collected at six time delays, ranging from 4 ns to 1.9 ms. The DED map (MbCO photoproduct–MbCO) at 4 ns shows a clear loss of the CO ligand caused by the photolysis. A CO* docking site is identified in the distal heme pocket, in the region where CO* has been observed in the low temperature photolysis studies ***(76–78)***. The docking site is absent in the 1 μs map indicating that the ligand has moved out of the distal pocket. The heme iron is displaced out of the heme plane whereas the distal histidine His64 moved inward, towards the location of the bound ligand. Small DED features observed along the E and F helices that surround the heme indicate that a more global structural relaxation also occurred, at least partially, by 4 ns.

The subsequent, more comprehensive study ***(16)*** that included 14 time delays, ranging from 1 ns to 1.9 ms, confirmed the initial findings and revealed more details about the ligand migration pathway, changes at the heme and protein relaxation. The ligand photodissociation was estimated to 40%. The iron motion, heme buckling and rotation, His64 swing, and initial displacement of the F and E helices have already occurred by 1 ns (*see* **Fig. 12**). Half of the photodissociated CO* molecules is detected at the distal docking site at 1 ns. The half-life of this site was estimated to approx 80 ns. A second CO* docking

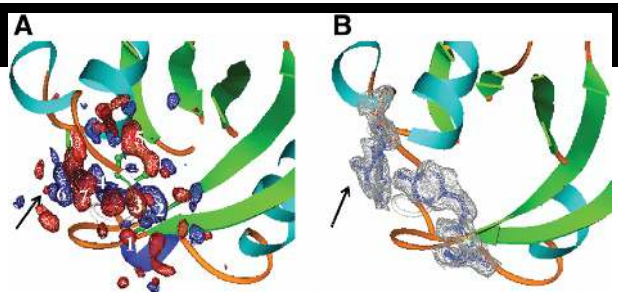

Fig. 11. **(A)** Time-independent difference map of an intermediate extracted from 15 time-points collected on the PYP ***(28)***. Features 1,3,5,7: negative DED for the pCA chromophore and Arg52; features 2,4,6: corresponding positive DED features. Dark-state structure of the pCA chromophore shown in green. **(B)** Extrapolated, conventional electron density map (gray) covering the pCA chromophore and Arg52 (blue structures). Arrows in **(A)** and **(B)** extrapolated electron density is present at the position of no or little DED in **(A)**.

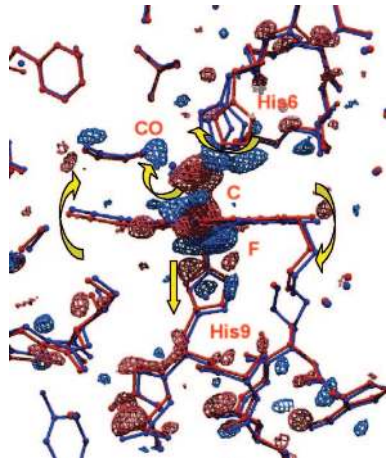

Fig. 12. DED map of the heme region at 1 ns following ligand photodissociation ***(16)***. The map is contoured at ± 3.5 σ and ± 7 σ. The red features represent negative electron density (loss of electrons) and the blue features positive density (gain of electrons). The arrows indicate observed structural changes: motion of the CO ligand to a docking site CO* in the distal pocket, downward motion of the iron, proximal histidine His93 and the F-helix, and swing of the distal histidine His64. The MbCO model is shown in red, deoxy Mb model in blue.

site was also detected, located on the proximal side of the heme. This is the so-called Xe1 site, one of four hydrophobic cavities where Xe is observed under pressure. The peak occupancy of this site of 20% is reached at about 100 ns and its half-life is estimated to about 10 μs.

The most recent ns and sub-ns MbCO TR experiments were conducted on two mutants. The ns experiment involved a triple mutant (Leu29(B10)Tyr, His64(E7)Gln, Thr67(E10)Arg), denoted YQR, and followed structural changes between 3 ns and 3 ms after the CO photodissociation ***(17)***. The loss of bound CO, tilt of the heme, swinging motion of Tyr-29(B10), and migration of CO* to the more remote docking site Xe4, located on the distal side of the heme, were all detected by 3 ns. By 316 ns, CO* has reached the proximal Xe1 site, similar as in wild-type myoglobin ***(18)***. Structural changes in the distal E-helix and CD-turn regions are found in this case to lag significantly (100–300 ns) behind local changes in the heme region. These results establish a structural basis for the extended time-course of the protein conformational relaxation observed by TR spectroscopy ***(10,11)***.

The first sub-ns TR experiment was conducted recently at the ID09 beamline, ESRF ***(13)***. The L29F mutant of MbCO was chosen because TR IR spectroscopy revealed a short-lived intermediate, with a lifetime of 140 ps. The observed structural changes at 100 ps involve large displacements of the side chains Phe29 and His64 to accommodate CO* at the primary, distal docking site, as well as more subtle correlated rearrangements throughout the entire protein. By 1 ns, CO* has migrated to the more distant Xe4 distal site and by 32 ns it moved to the proximal Xe1 site where it persists for microseconds.

3.6.2. Photoactive Yellow Protein

The photoactive yellow protein (PYP), a blue light photoreceptor with a bright yellow color and a molecular weight of 14.8 kD, was first identified by Meyer ***(85)*** in the halophilic bacterium *Ectothiorodospira halophila* (now called *Halorhodospira halophila*). It is a paradigm for light triggered reactions in living organisms and is most likely involved in the phototactic behavior of this bacterium ***(86)***. Upon illumination with blue light PYP enters a photocycle. The central chromophore, para-coumaric acid (pCA), changes its configuration from *trans* to *cis*. The consequent conformational change of the chromophore causes the protein to relax through numerous intermediates, with lifetimes ranging from sub-ps to 100 ms, to the dark state ***(5)***. The photocycle has been extensively studied by spectroscopy (*see*, e.g., **ref. *87*** for a review) and conventional crystallography using trapping methods ***(81)***.

The first TR experiment on PYP followed the relaxation from a photostationary state, produced by a 100 ms exposure to laser light ***(21)***. One Laue data set was collected with a 10 ms X-ray exposure time, 2 ms after the laser was switched off. The major observed structural change involves a swing of the pCA chromophore head towards the surface of the protein and correlated displacement of the adjacent residue Arg52 into the solvent.

The first ns TR crystallographic experiment on PYP by Perman et al. ***(22)*** revealed the structure of an intermediate populated at about 1 ns. The pattern of positive and negative DED features showed the *trans* to *cis* isomerization of the pCA chromophore already at 1ns, in accordance with results from TR spectroscopy ***(7)***. However, refined atomic structures of the early intermediate and those populated in the ns to µs time region are still missing.

Closely-spaced data sets in the time region from early µs to ms, following phototriggering by ns laser pulses, were collected recently at the APS beamline 14-ID ***(28)***. At the beginning of the analyzed time range, roughly 15% of the molecules were photo-activated. As demonstrated by mock data ***(27)***, this is sufficient for a successful analysis. The structures of two late intermediates in the photocycle were determined using the SVD-driven analysis described in **Subheadings 3.5.3–3.5.9**. The structures of the two late intermediates are similar to each other. They are also similar but not identical to the structure derived from the relaxation of the photostationary state mentioned previously. Detailed differences include the conformation of Tyr42, which has a different orientation in earlier time-points, and Arg52, which shows a double conformation in the pulsed experiment rather than a single conformation evident in the photostationary state. This study shows that an SVD-based analysis can be applied to real data and intermediates can be separated from an admixture. The photocycle of PYP is likely to be characterized completely in the near future on the time-scale from 100 ps to 1 s.

3.7. Conclusions and Future Outlook

With the demonstrated ability to detect small structural changes even at relatively low levels of reaction initiation (15 to 40%), TR crystallography has completed the phase of feasibility studies. Further improvements of the X-ray sources and optics at the third-generation synchrotrons and continuing advances in the development of methods for data analysis, such as the SVD-based analysis, provide us with the opportunity to expand the application of this technique beyond the first test cases, like myoglobin and PYP.

The major challenge in applying the technique to new systems of wider biological interest is to find a suitable and efficient method for the reaction initiation. Whereas the use of pulsed lasers is straightforward for a broad family of proteins containing a chromophore, like heme proteins and photoreceptors, other systems, like enzymes, require more system-specific efforts to determine a suitable caging method. Even irreversible processes can be considered, as improvements in the X-ray flux at the existing third-generation sources and the proposed next-generation, substantially more intense X-ray sources, such as the X-ray free-electron laser (XFEL) ***(88,89)***, will minimize the need for signal averaging and therefore the number of crystals required. The increased X-ray

flux will also allow the use of smaller crystals, down to μm and possibly sub-μm size. This will help to lower the diffusion barrier and enable diffusion triggering for reactions faster than presently possible given the crystal sizes used today.

Other important frontiers for the ultra-fast TRX involve further improvements in time resolution, the read-out time of the X-ray area detectors, methods for the determination of structures of intermediates and reaction mechanism, and in combining the TR technique with computational approaches. A considerable effort is given to the development of ultra-fast hard X-ray sources, such as the hard X-ray FEL mentioned earlier. In this device, extremely bright, fully coherent X-ray pulses of ~100 fs duration are to be generated, with peak brilliance many orders of magnitude higher than presently available at the third generation synchrotrons. This will provide an opportunity to explore important biological processes that involve events that occur on the fs time scale, such as photosynthesis. The development of large area pixel-array detectors with readout times in the sub-μs time scale ***(90)*** will greatly reduce the need for repeated pump-probe cycles. It will permit following a reaction in real-time by synchronizing a single reaction initiation with multiple cycles of X-ray exposure and detector readout.

The application of the SVD method to extract structures of time-independent intermediates from measured time-dependent data and the development of the *posterior* analysis for identification of possible reaction mechanism, clearly represent significant advances in the analysis of TR data. Further improvements of these methods as well as exploring new avenues in the TR data analysis ***(91)*** are the major goals in TRX. As discussed in the **Subheading 1.**, the ultimate goal of TRX is to provide structures of intermediate states that correspond to the energy minima on the potential energy surface of the system. However, to describe a reaction pathway completely, the characteristics of unstable transition states between the intermediates have to be known, as well as these states actually determine the reaction rates. Combining the experimental results from TRX with computational and theoretical approaches will greatly facilitate achievement of this goal. The high-resolution structures of intermediates from TRX provide solid constraints for methods such as free-energy perturbation simulations ***(92)*** and nudged elastic band calculations ***(93)*** in an effort to completely characterize the reaction pathways.

4. Notes

1. Time-independent DED maps of intermediates are determined in the following way. Preliminary concentrations of each intermediate I_j are calculated from a candidate mechanism by solving the system of coupled differential equations. They are then used to fit the significant rSV globally. In this nonlinear fitting

process the k are varied to match the magnitude of the observed vector elements $v(t)_n^{obs}$:

$$s_n^2 v(t)_n^{obs} \approx v(t)_n^{fit} = s_n^2 \cdot \sum_{j=1}^{J} E_{nj} \cdot I_j(k,t) \tag{4}$$

The fit is weighted by the square of the corresponding singular value s_n^2. The E_{nj} are linear fit parameters that have to be computed for each intermediate j and each singular vector n. The E_{nj} bring the concentrations to the (unknown) scale of the rSV.

Once the scale factors E_{nj} are determined, the time-independent DED for the j_{th} intermediate $\Delta\rho_{Ij}$ is computed using the significant singular values s_n, significant left singular vectors $\boldsymbol{u}_n$ and the scale factors E_{nj} :

$$\Delta\rho_{Ij} = \sum_{j=1}^{s} \boldsymbol{u}_n \cdot s_n \cdot E_{n,j} \tag{5}$$

2. Extrapolated, conventional electron density maps for intermediates are determined in the following way.
   The extracted time-independent DED map $\Delta\rho_{Ij}$ is Fourier transformed and difference SF $\Delta\boldsymbol{F}_j$ are obtained. A multiple f of the difference SF vector is added to the calculated SF vector of the dark state $\boldsymbol{F}_D{}^{calc}$:

$$\boldsymbol{F}_j^{ext} = \boldsymbol{F}_D^{calc} + f\Delta\boldsymbol{F}_j \tag{6}$$

   The extrapolated map for the j_{th} intermediate is then calculated from the extrapolated structure factors $\boldsymbol{F}_j^{ext}$. The factor f is adjusted, so that the negative density features initially observed on prominent atoms of the dark structure in the extrapolated map just vanish. The atomic model can be built into this extrapolated map and refined by conventional methods against the $/\,\boldsymbol{F}_j^{ext}\,/$. The residual $\boldsymbol{F}_j^{ext} - \boldsymbol{F}_j^{calc}$ difference map (the $\boldsymbol{F}_j^{calc}$ are SF determined from the refined model of the intermediate j), indicates if some electron density features are still not interpreted. This may be the case, if a wrong mechanism is used or if states, which are populated at earlier times where no data are available, are mixed in.
3. Posterior analysis is performed in the following way. SF $\boldsymbol{F}_{Ij}$ are calculated from the structures of the initial dark state and intermediates. Difference SF $\Delta\boldsymbol{F}_{Ij}$ are determined by subtracting the dark state structure factors $\boldsymbol{F}^D$ from those of the intermediates ($\Delta\boldsymbol{F}_{Ij} = \boldsymbol{F}_{Ij} - \boldsymbol{F}^D$). The $\Delta\boldsymbol{F}_{Ij}$ are used to calculate time independent difference maps, $\Delta\rho_{Ij}^{calc}$, for each intermediate. Time-dependent DED maps are then calculated on the absolute scale using the rate k dependent concentrations I_j of the intermediates from **Note 1**:

$$\Delta\rho(k,t)^{calc} = \sum_{j=1}^{J} I_j(k,t) \cdot \Delta\rho_{Ij}^{calc} \tag{7}$$

   The $\Delta\rho(k,t)^{calc}$ must be represented on the same three-dimensional grid as the observed, SVD-flattened DED maps $\Delta\rho(t)^{SVD}$. Hence, the observed DED values

$\Delta\rho_m(t)^{SVD}$ can be compared to the calculated $\Delta\rho_m(k,t)^{calc}$ at every grid point m. **Equation 8** is used as a kernel of a fit routine to refine the rate coefficients k for the mechanism. The inner loop sums over all M grid points in a particular map, whereas the outer loop sums over all T available maps.

$$\sum_{t=1}^{T}\sum_{m=1}^{M}\frac{1}{\left\langle\left|\Delta\rho(t)\right|^{SVD}\right\rangle}\left(\Delta\rho_m(t)^{SVD}-C_{RI}\cdot\Delta\rho_m(k,t)^{calc}\right)^2 \tag{8}$$

C_{RI} is a linear fit parameter, which scales the calculated DED maps to the observed DED maps. C_{RI} is equivalent to the concentration of activated molecules in the reaction and therefore represents the extent of reaction initiation. The fit is weighted by the average of the observed absolute difference electron density $\langle|\Delta\rho(t)^{SVD}|\rangle$. This ensures that all DED maps, with weak or strong signal, are considered on an equal footing. To reduce the effect of noise on the fit, only the grid points below or above some σ value should be used. A cutoff of $\pm 2\sigma$ is a reasonable choice.

Acknowledgments

MS was supported by the Deutsche Forschungsgemeinschaft, SFB 533 and HI was supported by the Korea Research Foundation Grant (KRF-2004-003-C00100). RP and VŠ were supported by the NIH/NCRR grant RR07707.

References

1. Moffat, K. and Henderson, R. (1995) Freeze trapping of reaction intermediates. *Curr. Opin. Struct. Biol.* **5,** 656–663.
2. Schlichting, I. and Chu, K. (2000) Trapping intermediates in the crystal: ligand binding to myoglobin. *Curr. Opin. Struct. Biol.* **10,** 744–752.
3. Stoddard, B. L. (2001) Trapping reaction intermediates in macromolecular crystals for structural Analysis. *Methods in Enzymology* **24,** 125–138.
4. Ursby, T., Weik, M., Fioravanti, E., Delarue, M., Goeldner, M., and Bourgeois, D. (2002) Cryophotolysis of caged compounds: a technique for trapping intermediate states in protein crystals. *Acta Cryst.* **D58,** 607–614.
5. Hellingwerf, K., Hendriks, J., and Gensch, T. (2003) On the configurational and conformational changes in photoactive yellow protein that leads to signal generation in *Ectothiorhodospira halophila*. *J Biol. Phys.* **28,** 295–412.
6. Brudler, R., Rammelsberg, R., Woo, T. T., Getzoff, E. D., and Gerwert, K. (2001) Structure of the I_1 early intermediate of photoactive yellow protein by FTIR spectroscopy. *Nature Struct. Biol.* **8,** 265–270.
7. Ujj, L., Devanathan, S., Meyer, T. E., Cusanovich, M. A., Tollin, G., and Atkinson, G. H. (1998) New photocycle intermediates in the photoactive yellow protein from *Ecothiorhodospira halophila*: picosecond transient absorption spectroscopy. *Biophys. J.* **75,** 406–412.
8. Haupts, U., Tittor, J., and Oesterhelt, D. (1999) Closing in on bacteriorhodopsin: progress in understanding the molecule. *Annu. Rev. Biophys. Biomol. Struct.* **283,** 67–99.

9. Mizutani, Y. and Kitagawa, T. (2001) Ultrafast structural relaxation of myoglobin following photodissociation of carbon monoxide probed by time-resolved resonance Raman cpectroscopy. *J. Phys. Chem. B* **105,** 10,992–10,999.
10. Jackson, T. A., Lim, M., and Anfinrud, P. (1994) Complex nonexponential relaxation in myoglobin after photodissociation of MbCO: measurement and analysis from 2 ps to 56 μs. *Chem. Phys* **180,** 131–140.
11. Ansari, A., Jones, C. M., Henry, E. R., Hofrichter, J., and Eaton, W. A. (1994) Conformational relaxation and ligand binding in myoglobin. *Biochemistry* **33,** 5128–5145.
12. Xie, X. and Simon, J. D. (1991) Protein conformational relaxation following photodissociation of co from carbonmonoxymyoglobin–picosecond circular-dichroism and absorption studies. *Biochemistry* **30,** 3682–3692.
13. Schotte, F., Lim, M., Jackson, T. A., Smirnov, A. V., Soman, J., Olson, J. S., Phillips, G. N. J., Wulff, M., and Anfinrud, P. (2003) Watching a protein as it functions with 150ps time-resolved X-ray crystallography. *Science* **300,** 1944–1947.
14. Krinsky, S., Fundamentals of Hard X-ray Synchrotron Radiation Sources, in *Third-Generation Hard X-ray Synchrotron Radiation Sources*, Mills, D., Ed., John Wiley & Sons, Inc., New York (2002).
15. Ren, Z., Bourgeois, D., Helliwell, J. R., Moffat, K., Šrajer, V., and Stoddard, B. L. (1999) Laue crystallography: coming of age. *J. Synchrotron Rad.* **6,** 891–917.
16. Šrajer, V., Ren, Z., Teng, T.-Y., Schmidt, M., Ursby, T., Bourgeois, D., Pradervand, C., Schildkamp, W., Wulff, M., and Moffat, K. (2001) Protein conformational relaxation and ligand migration in myoglobin: a nanosecond to millisecond molecular movie from time-resolved Laue X-ray diffraction. *Biochemistry* **40,** 13,802–13,815.
17. Bourgeois, D., Vallone, B., Schotte, F., Arcovito, A., Miele, A. E., Sciara, G., Wulff, M., Anfinrud, P., and Brunori, M. (2003) Complex landscape of protein structural dynamics unveiled by nanosecond Laue crystallography. *Proc. Natl. Acad. Sci.* **100,** 8704–8709.
18. Šrajer, V., Teng, T.-Y., Ursby, T., Pradervand, C., Ren, Z., Adachi, S., Schildkamp, W., Bourgeois, D., Wulff, M., and Moffat, K. (1996) Photolysis of the carbon monoxide complex of myoglobin: nanosecond time-resolved crystallography. *Science* **274,** 1726–1729.
19. Neutze, R., Pebay-Peyroula, E., Edman, K., Royant, A., Navarro, J., and Landau, E. M. (2002) Bacteriorhodopsin: a high resolution structural view of vectorial proton transport. *Biochim. Biophys. Acta* **1565**, 144–167.
20. Ren, Z., Perman, B., Šrajer, V., Teng, T.-Y., Pradervand, C., Bourgeois, D., Schotte, F., Ursby, T., Kort, R., Wulff, M., and Moffat, K. (2001) A molecular movie at 1.8 A resolution displays the photocycle of photoactive yellow protein, a eubacterial blue-light receptor, from nanoseconds to seconds. *Biochemistry* **40,** 13,788–13,801.
21. Genick, U. K., Borgstahl, G. E., Ng, K., Ren, Z., Pradervand, C., Burke, P. M., Šrajer, V., Teng, T.-Y., Schildkamp, W., McRee, D. E., Moffat, K., and Getzoff, E. D. (1997) Structure of a protein photocycle intermediate by millisecond time-resolved crystallography. *Science* **275,** 1471–1475.

22. Perman, B., Šrajer, V., Ren, Z., Teng, T-.Y., Pradervand, C., Ursby, T., Bourgeois, D., Schotte, F., Wulff, M., Kort, R., Hellingwerf, K., and Moffat, K. (1998) Energy transduction on the nanosecond time scale: early structural events in a xanthopsin photocycle. *Science* **279,** 1946–1950.
23. Crosson, S. and Moffat, K. (2002) Photoexcited structure of a plant photoreceptor domain reveals a light-driven molecular switch. *Plant Cell* **14,** 1067–1075.
24. Karplus, M. (1999) In *Simplicity and Complexity in Proteins and Nucleic Acids*, (Frauenfelder, H., Deisenhofer, J., and Wolynes, P., eds.). Dahlem University Press, Belin, p. 139.
25. Moffat, K. (2001) Time-resolved biochemical crystallography: a mechanistic perspective. *Chem. Rev.* **101,** 1569–1581.
25a. Steinfeld, J. I., Francisco, J. S., and Haase, W. L. (1989) C*hemical Kinetics and Dynamics*. Prentice Hall, Englewood Cliffs, NJ.
26. Moffat, K. (1989) Time-Resolved Macromolecular Crystallography. *Annu. Rev. Biophys. Biophys. Chem.* **18,** 309–332.
27. Schmidt, M., Rajagopal, S., Ren, Z., and Moffat, K. (2003) Application of singular value decomposition to the analysis of time-resolved macromolecular x-ray data. *Biophys. J.* **84,** 2112–2129.
28. Schmidt, M., Pahl, R., Šrajer, V., Anderson, S., Ren, Z., Ihee, H., and Moffat, K. (2004) Protein kinetics: structures of intermediates and reaction mechanism from time-resolved x-ray data. *Proc. Natl. Acad. Sci.* **101,** 4799–4804.
29. Rajagopal, S., Schmidt, M., Anderson, S., Ihee, H., and Moffat, K. (2004) Analysis of experimental time-resolved crystallographic data by singular value decomposition. *Acta Cryst. D* **60,** 860–871.
30. Abdel-Meguid, S. S., Jeruzalmi, D., and Sanderson, M. R. (1996) Preliminary characterization of crystals. In *Crystallographic methods and Protocols*, Vol. 56 (Jones, C., Mulloy, B., and Sanderson, M. R., eds.). Humana Press, Totowa, NJ, pp. 55–86.
31. Carrell, H. L. and Glusker, J. P. (2001) *Crystallography of Biological Macromolecules*, Kluwer Academic Publishers, Dordrecht, The Netherlands.
32. Ren, Z. and Moffat, K. (1995) Quantitative analysis of synchrotron laue diffraction patterns in macromolecular crystallography. *J. Appl. Cryst.* **10,** 461–481.
33. Ren, Z. and Moffat, K. (1995) Deconvolution of energy overlaps in laue diffraction. *J. Appl. Cryst.* **28,** 482–493.
34. Campbell, J. W. (1995) LAUEGEN, an X-windows-based program for the processing of Laue diffraction data. *J. Appl. Cryst.* **28,** 228–236.
35. Arzt, S., Campbell, J. W., Harding, M. M., Hao, Q., and Helliwell, J. R. (1999) LSCALE - the new normalization, scaling and absorption correction program in the Daresbury Laue software suite. *J. Appl. Cryst.* **32,** 554–562.
36. Wakatsuki, S. (1993) LEAP, Laue evaluation analysis package, for time-resolved protein crystallography, in *CCP4 Study Weekend Proceedings: Data Collection and Processing*, Sawyer, L., Isaacs, N. W., and Bailey, S., eds., CLRC Daresbury, Warrington, UK, pp. 71–79.
37. Bourgeois, D., Nurizzo, D., Kahn, R., and Cambillau, C. (1998) An integration routine based on profile fitting with optimized fitting area for the evaluation of

weak and/or overlapped two-dimensional Laue or monochromatic patterns. *J. Appl. Cryst.* **31,** 22–35.
38. Ren, Z. (2003) Precognition, commercial package; www.renzresearch.com.
39. Scott, W. G., Murray, J. B., Arnold, J. R. P., Stoddard, B. L., and Klug, A. (1996) Capturing the structure of a catalytic RNA intermediate: the hammerhead ribozyme. *Science* **274,** 2065–2069.
40. Singer, P. T., Smalas, A., Carty, R. P., Mangel, W. F., and Sweet, R. M. (1993) The hydrolytic water molecule in trypsin revealed by time-resolved Laue crystallography. *Science* **259,** 669–673.
41. Fulop, V., Phizackerley, R. P., Soltis, S. M., Clifton, I. J., Wakatsuki, S., Erman, J., Hajdu, J., and Edwards, S. L. (1994) Laue diffraction study on the structure of cytochrome c peroxidase compound I. *Structure* **2,** 201–208.
42. Bolduc, J. M., Dyer, D. H., Scott, W. G., Singer, P., Sweet, R. M., Koshland, D. E. J., and Stoddard, B. L. (1995) Mutagenesis and Laue structures of enzyme intermediates: isocitrate dehydrogenase. *Science* **268,** 1312–1318.
43. Gouet, P., Jouve, H. M., Williams, P. A., Andersson, I., Andreoletti, P., Nussaume, L., and Hajdu, J. (1996) Ferryl intermediates of catalase captured by time-resolved Weisenberg crystallography and UV-VIS spectroscopy. *Nature Struct. Biol.* **3,** 951–956.
44. Helliwell, J. R., Nieh, Y. P., Raftery, J., Cassetta, A., Habash, J., Carr, P. D., Ursby, T., Wulff, M., Thompson, A. W., C., N. A., and Hadener, A. (1998) Time-resolved structures of hydroxymethylbilane synthase (Lys59Gln mutant) as it is loaded with substrate determined by Laue diffraction. *J. Chem. Soc. Faraday Trans.* **94,** 2615–2622.
45. Schlichting, I. and Goody, R. S. (1997) Triggering methods in crystallographic enzyme kinetics. *Methods in Enzymology* **277**, 467–490.
46. Chen, Y. (1994) PhD. Thesis. Cornell University, Ithaca, NY.
47. Hori, T., Moriyama, H., Kawaguchi, J., Hayashi-Iwasaki, Y., Oshima, T., and Tanaka, N. (2000) The initial step of the thermal unfolding of 3-isopropylmalate dehydrogenase detected by the temperature-jump Laue method. *Protein Engineering* **13,** 527–533.
48. McCray, J. A. and Trentham, D. R. (1989) Properties and uses of photoreactive caged compounds. *Annu. Rev. Biophys. Biophys. Chem.* **18**, 239–270.
49. Corrie, J. E. T., and Trenhtam, D. R. (1993) *Biological Applications of Photochemical Switches*, Vol. 2, Wiley, New York, NY.
50. Schlichting, I., Almo, S. C., Rupp, G., Wilson, K., Petratos, K., Lentfer, A., Wittinghofer, A., Kabash, W., Pai, E. F., Petsko, G. A., and Goody, R. S. (1990) Time-resolved X-ray crystallographic study of the conformational change in Ha-ras p21 protein on GTP hydrolysis. *Nature* **345,** 309–315.
51. Stoddard, B. L., Koenigs, P., Porter, N., Petratos, K., Petsko, G. A., and Ringe, D. (1991) Observation of the light-triggered binding of pyrone to chymotrypsin by Laue X-ray crystallography. *Proc. Natl. Acad. Sci.* **88,** 5503–5507.
52. Duke, E. M. H., Wakatsuki, W., Hadfield, A., and Johnson, L. N. (1994) Laue and monochromatic diffraction studies on catalysis in phosphorylase b crystals. *Protein Sci.* **3,** 1178–1196.

53. Stoddard, B. L., Cohen, B. E., Brubaker, M., Mesecar, A. D., and Koshland, D. E. J. (1998) Millisecond Laue structures of an enzyme-product complex using photocaged substrate analogs. *Nature Struct. Biol.* **5,** 891–897.
54. Chen, Y., Šrajer, V., Ng, K., LeGrand, A., and Moffat, K. (1994) Optical monitoring of protein crystals in time-resolved x-ray experiments— microspectrophotometer design and performance. *Rev. Sci. Instrum.* **65,** 1506–1511.
55. Hadfield, A. and Hajdu, J. (1993) A fast and portable microspectrophotometer for protein crystallography. *J. Appl. Cryst.* **26,** 839–842.
56. Sakai, K., Matsui, Y., Kouyama, T., Shiro, Y., and Adachi, S.-I. (2002) Optical monitoring of freeze trapped reaction intermediates in protein crystals: A microspectrophotometer for cryogenic protein crystallography. *J. Appl. Cryst.* **35,** 270–273.
57. Bourgeois, D., Vernede, X., Adam, V., Fioravanti, E., and Ursby, T. (2002) A microspectrophotometer for UV-visible absorption and fluorescence studies of protein crystals. *J. Appl. Cryst.* **35,** 319–326.
58. Anderson, S., Šrajer, V., Pahl, R., Rajagopal, S., Schotte, F., Anfinrud, P., Wulff, M., and Moffat, K. (2004) Chromophore conformation and the evolution of tertiary structural changes in photoactive yellow protein. *Structure* **12,** 1039–1045.
59. Bourgeois, D., Ursby, T., Wulff, M., Pradervand, C., LeGrand, A., Schildkamp, W., Laboure, S., Šrajer, V., Teng, T.-Y., Roth, M., and Moffat, K. (1996) Feasibility and realization of single-pulse laue diffraction on macromolecular crystals at ESRF. *J. Synchrotron Rad.* **3,** 65–74.
60. Schotte, F., Techert, S., Anfinrud, P., Šrajer, V., Moffat, K., and Wulff, M. (2002) Picosecond structural studies using pulsed synchrotron radiation. In *Third-Generation Hard X-Ray Synchrotron Radiation Sources*. (Mills, D., ed.). John Wiley & Sons, Inc., New York, NY, pp. 345–401.
61. Knapp, J. E., Šrajer, V., Pahl, R., and Royer, W. E. J. (2004) Immobilization of *Scapharca* HbI crystals improves data quality of a time-resolved crystallographic experiment. *Micron.* **35,** 107–108.
62. Šrajer, V., Crosson, S., Schmidt, M., Key, J., Schotte, F., Anderson, S., Perman, B., Ren, Z., Teng, T.-Y., Bourgeois, D., Wulff, M., and Moffat, K. (2000) Extraction of accurate structure factor amplitudes from Laue data: wavelength normalization with wiggler and undulator X-ray sources. *J. Synchrotron Rad.* **7,** 236–244.
63. Bourgeois, D., Wagner, U., and Wulff, M. (2000) Towards automated Laue data processing: application to the choice of optimal X-ray spectrum. *Acta Cryst.* **D56,** 973–985.
64. Helliwell, J. R. (1992) *Macromolecular Crystallography With Synchrotron Radiation*. Cambridge University Press, Cambridge, UK.
65. Drenth, J. (1999) *Principles of Protein X-Ray Crystallography*, Springer, New York, NY.
66. Henderson, R., and Moffat, J. K. (1971) The difference Fourier technique in protein crystallography: errors and their treatment. *Acta Cryst. B* **27,** 1414–1420.
67. Ursby, T., and Bourgeois, D. (1997) Improved estimation of structure-factor difference amplitudes from poorly accurate data. *Acta Cryst. A* **53,** 564–575.

68. McRee, D. E. (1999) *Practical Protein Crystallography*, Academic Press, San Diego, CA.
69. Jones, T. A., Bergdoll, M., and Kjeldgaard, M., O. (1990) A macromolecular modeling environment. In *Crystallographic and Modeling Methods in Molecular Design*. (Bugg, C. and Ealick, S., eds.). Springer-Verlag Press, New York, NY, pp. 189–195.
70. Henry, E. R. and Hofrichter, J. (1992) Singular value decomposition: Application to analysis of experimental data. *Methods in Enzymology* **210,** 129–192.
71. Carson, M. (1997) Ribbons. In *Methods in Enzymology*, Vol. 277. (Sweet, R. M., and Carter, C. W., eds.) Academic Press, pp. 493–505.
72. Hajdu, J., Neutze, R., Sjogren, T., Edman, K., Szoke, H., Wilmouth, R. C., and Wilmot, C. M. (2000) Analyzing protein functions in four dimensions. *Nature Struct. Biol.* **7,** 1006–1012.
73. Moffat, K. (1998) Time-Resolved Crystallography. *Acta Cryst. A* **54,** 833–841.
74. Schlichting, I., Berendzen, J., Chu, K., Stock, A. M., Maves, S. A., Benson, D. E., Sweet, R. M., Ringe, D., Petsko, G. A., and Sligar, S. G. (2000) The catalytic pathway of cytochrome $P450_{cam}$ at atomic resolution. *Science* **287,** 1615–1622.
75. Berglund, G. I., Carlsson, G. H., Smith, A. T., Szoke, H., Henriksen, A., and Hajdu, J. (2002) The catalysis pathway of horseradish peroxidase at high resolution. *Nature* **417,** 463–468.
76. Schlichting, I., Berendzen, J., Phillips, G. N., and Sweet, R. M. (1994) Crystal structure of photolyzed carbonmonoxy-myoglobin. *Nature* **371,** 808–812.
77. Teng, T. Y., Šrajer, V., and Moffat, K. (1994) Photolysis-induced structural changes in single crystals of carbonmonoxymyoglobin at 40K. *Nature Struct. Biol.* **1,** 701–705.
78. Teng, T. Y., Šrajer, V., and Moffat, K. (1997) Initial trajectory of carbon monoxide after photodissociation from myoglobin at cryogenic temperatures. *Biochemistry* **36,** 12,087–12,100.
79. Chu, K., Vojtechovsky, J., McMahon, B. H., Sweet, R. M., Berendzen, J., and Schlichting, I. (2000) Structure of a ligand-binding intermediate in wild-type carbonmonoxy myoglobin. *Nature* **403,** 921–923.
80. Ostermann, A., Waschipky, R., Parak, F. G., and Nienhaus, G. U. (2000) Ligand binding and conformational motions in myoglobin. *Nature* **404,** 205–208.
81. Genick, U. K., Soltis, S. M., Kuhn, P., Canestrelli, I. L., and Getzoff, E. D. (1998) Structure at 0.85 angstrom resolution of an early protein photocycle intermediate. *Nature* **392,** 206–209.
82. Kendrew, J. C., Dickerson, R. E., Strandberg, B. E., Hart, R. G., Davies, D. R., Phillps, D. C. and Shore, V. C. (1960) Structure of myoglobin. A three-dimensional Fourier synthesis at 2 A resolution. *Nature* **185**.
83. Ansari, A., Berendzen, J., Bowne, S. F., Frauenfelder, H., T., I. I. E., Sauke, T. B., Shyamsunder, E., and Young, R. D. (1985) Protein states and protein quakes. *Proc. Natl. Acad. Sci.* **82**, 5000–5004.
84. Kachalova, G. S., Popov, A. N., and Bartunik, H. D. (1999) A steric mechanism for inhibition of CO binding to heme proteins. *Science* **284,** 473–476.

85. Meyer, T. E. (1985) Isolation and characterization of soluble cytochromes, ferredoxins and other chromophoric proteins from the halophile phototrophic bacterium Ectothiorhodospira halophila. *Biochim. Biophys. Acta.* **806,** 175–183.
86. Sprenger, W. W., Hoff, W. D., Armitage, J. P., and Hellingwerf, K. J. (1993) The eubacterium Ectothiorhodospira halophila is negatively phototactic, with a wavelength dependence that fits the absorption spectrum of the photoactive yellow protein. *J. Bacteriol.* **175,** 3096–3104.
87. Cusanovich, M. A. and Meyer, T. E. (2003) Photactive yellow protein: a prototypic PAS domain sensory protein and development of a common signaling mechanism. *Biochemistry* **42,** 4759–4770.
88. Winick, H. (1995) The linac coherent light source (LCLS): A fourth generation light source using the SLAC linac. *J. Elec. Spec. Rel. Phenom.* **75,** 1–8.
89. Wiik, B. H. (1997) The TESLA project: an accelerator facility for basic science. *Nucl. Inst. Meth. Phys. Res. B* **398,** 1–17.
90. Rossi, G., Renzi, M., Eikenberry, E. F., Tate, M. W., Bilderback, D. H., Fontes, E., Wixted, R., Barna, S., and Gruner, S. M. (1999) Tests of a prototype pixel array detector for microsecond time-resolved X-ray diffraction. *J. Synchrotron Rad.* **6,** 1096–1105.
91. Rajagopal, S., Kostov, K., and Moffat, K. (2004) Analytical trapping: Extraction of time-independent structures from time-dependent crystallographic data. *J. Struct. Biol.*, in press.
92. Schweins, T., Langen, R., and Warshel, A. (1994) Why mutagenesis studies not located the general base in Ras P21. *Nature Struct. Biol.* **1,** 476–484.
93. Henkelman, G., Johannesson, G., and Jonsson, B. (2000) Methods for finding saddle points and minimum energy paths. In *Progress on Theoretical Chemistry and Physics.* (Schwartz, S. D., ed.). Kluwer Academic Publishers, Dordrecht, The Netherlands, p. 269.